Article

Current Biology

Presynaptic and postsynaptic determinants of claustro-cortical connectivity

Graphical abstract

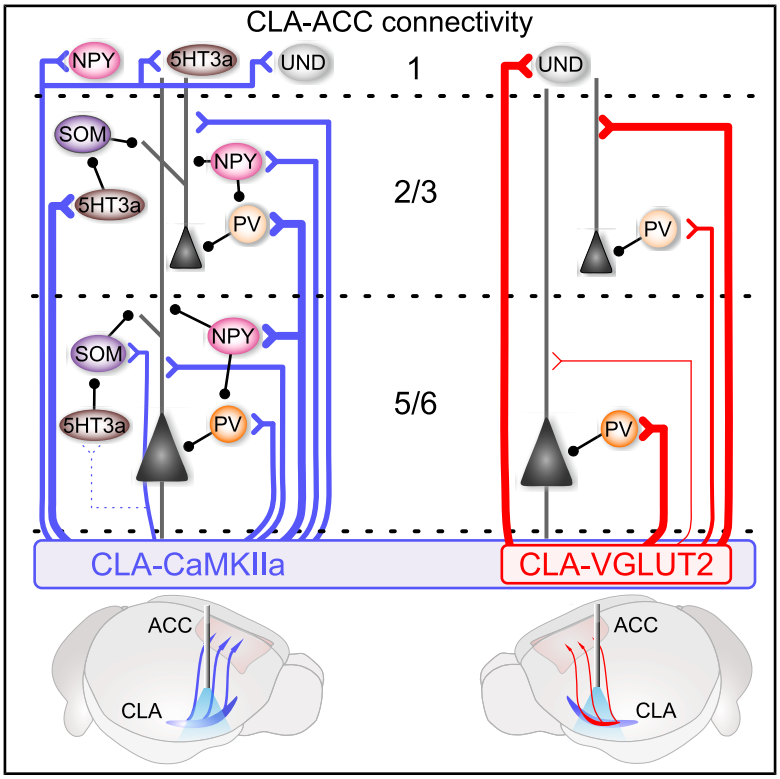

Highlights

- Claustrum activation drives excitation and inhibition throughout ACC layers
- Claustro-cortical axons target both pyramidal neurons and GABAergic interneurons
- VGLUT2 and CaMKIIa projections have distinct innervation profiles in ACC

Authors

Roberto de la Torre-Martínez, Zach Chia, Joseph Baxendale, Anna Tokarska, Johanna Frost-Nylén, George J. Augustine, Gilad Silberberg

Correspondence

roberto.de.la.torre.martinez@ki.se (R.d.l. T.-M.), gilad.silberberg@ki.se (G.S.)

In brief

de la Torre-Martínez et al. dissect the synaptic organization of claustro-cortical pathways using *in vivo* and slice recordings combined with optogenetics. By targeting two neuronal populations in the claustrum and five types of cortical neurons in different layers, they uncover the cellular and synaptic mechanisms for claustro-cortical signaling.

de la Torre-Martínez et al., 2025, Current Biology *35*, 3174–3190
July 7, 2025
https://doi.org/10.1016/j.cub.2025.05.056

CellPress

CellPress
OPEN ACCESS

Current Biology

Article

Presynaptic and postsynaptic determinants of claustro-cortical connectivity

Roberto de la Torre-Martínez,[1,5,*] Zach Chia,[1,2,3,5] Joseph Baxendale,[1] Anna Tokarska,[1] Johanna Frost-Nylén,[1] George J. Augustine,[2,4] and Gilad Silberberg[1,6,*]

[1]Department of Neuroscience, Karolinska Institutet, 17177 Stockholm, Sweden
[2]Lee Kong Chian School of Medicine, Nanyang Technological University, 11 Mandalay Road, Singapore 308232, Singapore
[3]School of Biological Sciences, Nanyang Technological University, 60 Nanyang Drive, Singapore 637551, Singapore
[4]Temasek Life Sciences Laboratory, National University of Singapore, 1 Research Link, Singapore 117604, Singapore
[5]These authors contributed equally
[6]Lead contact
*Correspondence: roberto.de.la.torre.martinez@ki.se (R.d.l.T.-M.), gilad.silberberg@ki.se (G.S.)
https://doi.org/10.1016/j.cub.2025.05.056

SUMMARY

The claustrum (CLA) is a thin and elongated brain structure that is located between the insula and lateral striatum and is implicated in a wide range of behaviors. It is characterized by its extensive synaptic connectivity with multiple cortical regions. While CLA projection neurons are glutamatergic, several studies have shown an inhibitory impact of CLA on its cortical targets, suggesting the involvement of inhibitory cortical interneurons. We employed both *in vivo* and *ex vivo* electrophysiology and optogenetics in mice to dissect the synaptic organization of projections from the CLA to the anterior cingulate cortex (ACC), a robust claustro-cortical pathway implicated in cognitive functions. Optogenetic stimulation of CLA neurons expressing calcium/calmodulin-dependent protein kinase II alpha (CaMKIIa) or vesicular glutamate transporter-2 (VGLUT2) evoked distinct multiphasic excitatory and inhibitory responses in the ACC that depended on the stimulated CLA neuron population and the recipient layer in the ACC. Stimulation of CLA-ACC axons evoked monosynaptic responses in pyramidal neurons and four types of molecularly defined interneurons. Synaptic responses were uniquely determined by the presynaptic CLA projection type, the recipient cortical layer, and the type of postsynaptic neuron, with interneurons displaying the highest specificity. This intricate organization of the CLA-ACC pathway explains the diverse and complex influence of CLA on cortical activity.

INTRODUCTION

The claustrum (CLA) is a brain structure located between the insula and striatum, which is highly interconnected with different cortical[1–22] and subcortical[9,22–28] brain regions. The extensive claustro-cortical connectivity has led to numerous hypotheses regarding its function.[10,29–39] The CLA has been suggested to be involved in sensorimotor functions,[40,41] salience reporting,[10,11,42–44] memory consolidation,[45] pain mediation,[36–38,46,47] attention,[48–50] regulation of cortical sleep waves,[27,39,51–54] and impulse control.[55] Central to these various functions is the dense connectivity with prefrontal cortical regions, in particular the anterior cingulate cortex (ACC).[11,18,20,21] The CLA and ACC are reciprocally connected,[11,49] with a robust CLA-ACC projection consisting of several types of presynaptic CLA neurons.[10,48,56]

Projections from CLA are glutamatergic, yet the net effect of CLA on targeted cortical regions is predominantly reported to be inhibitory.[27,45,48,57–62] Other work, however, showed that activation of specific CLA neurons expressing the vesicular glutamate transporter-2 (VGLUT2) increased neuronal activity in the prefrontal cortex,[50] suggesting that the impact of CLA on its cortical targets depends on the type of projection neurons. Indeed, CLA neurons are heterogeneous, containing subtypes expressing different electrophysiological[10,19,21,63] and molecular[48,56,64] properties, even among CLA neurons projecting to the same region.[10,11] Another factor that may contribute to the complex impact of CLA on its cortical targets is the specific connectivity with cortical GABAergic interneurons,[57,65,66] which are instrumental in shaping cortical activity.[67–72] Despite the major functional role assigned to the CLA-ACC pathway, very little is known about its synaptic organization and the properties of its pre- and postsynaptic neurons.

Here, we combined *in vivo* multiunit recordings in awake mice, *ex vivo* whole-cell recordings, optogenetics, and pharmacology to chart the detailed synaptic organization of the CLA-ACC pathway. We show that CLA photostimulation in awake mice produces diverse responses in the ACC with both excitation and inhibition, depending on the identity of the presynaptic CLA neuron type. Using *ex vivo* whole-cell recordings, we then show that cortical pyramidal neurons and GABAergic interneurons, including parvalbumin (PV)-, somatostatin (SOM)-, 5HT3a-, and neuropeptide-Y (NPY)-expressing interneurons, receive distinct synaptic input from the CLA.

Our results show that the synaptic connectivity from the CLA to the ACC is intricately organized according to the identities of pre- and postsynaptic neurons and their cortical laminar

CellPress
OPEN ACCESS

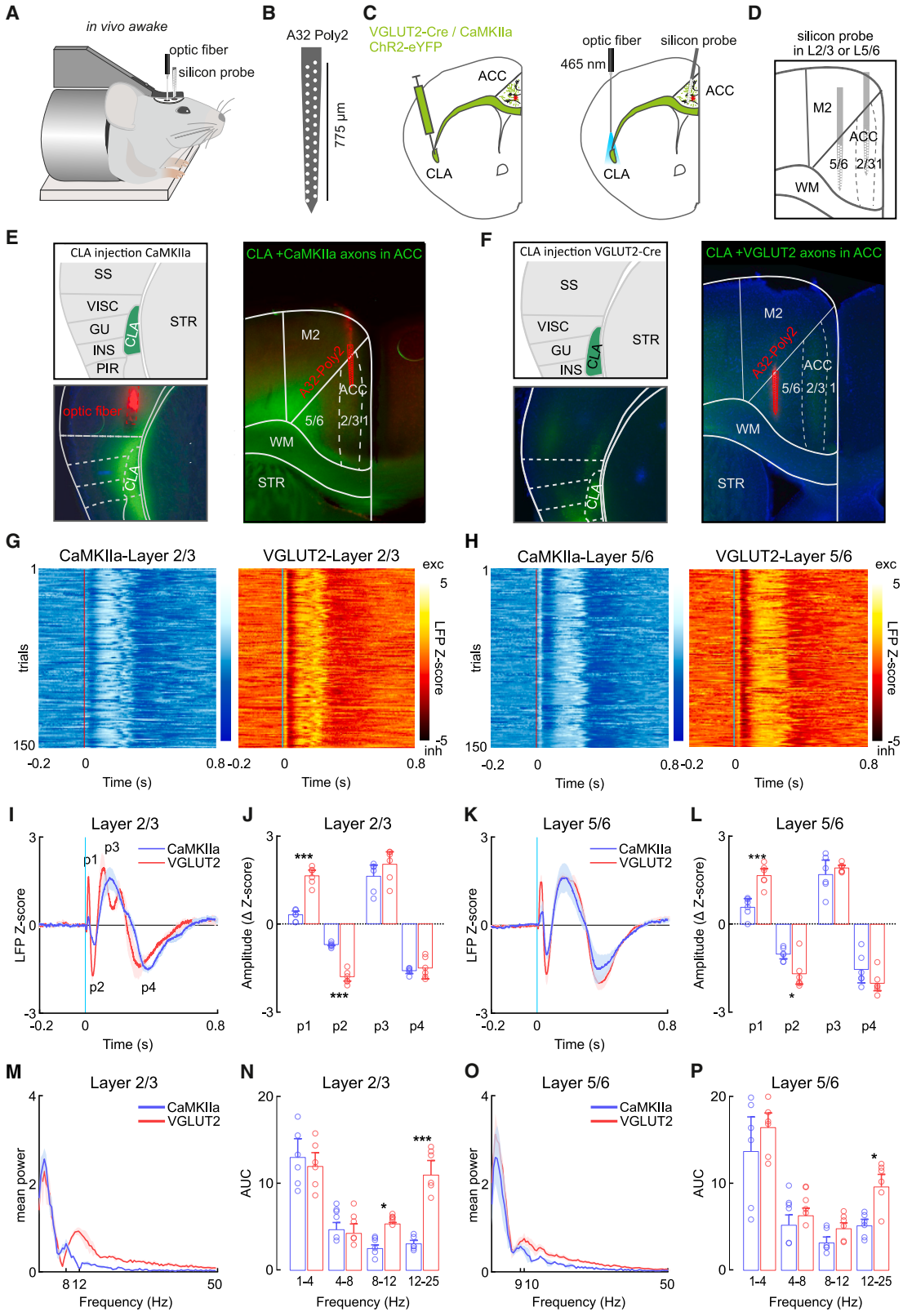

Figure 1. Activation of CLA-ACC neurons affects cortical activity in the ACC *in vivo*

(A) *In vivo* recordings performed in the mouse ACC with high-density silicon probes.

(B) Schematic of the 32-channel silicon probe (NeuroNexus A32-Poly 2).

(legend continued on next page)

locations. This precise synaptic organization of the CLA-ACC pathway explains the diversity observed in the functional impact of CLA on cortical dynamics.

RESULTS

In vivo activation of CLA induces multiphasic responses in the ACC

To characterize the impact of CLA projections on the ACC, we first recorded local field potentials (LFPs) in layers 2/3 and 5/6 of the ACC during optogenetic stimulation of CLA in awake, head-restrained mice (Figures 1A and 1B). Channelrhodopsin2 (ChR2) was expressed in CLA neurons using either a broad-acting promoter in calcium/calmodulin-dependent protein kinase II alpha (CaMKIIa)-expressing neurons (Figures 1C, 1E, and S1) or a specific Cre-dependent promoter only in VGLUT2-expressing neurons (STAR Methods; Figures 1C, 1E, and 1F). Whereas VGLUT2-expressing neurons constitute a specific subpopulation within CLA projection neurons,[48,50,56] CaMKIIa labels the vast majority of excitatory CLA neurons.[37,73,74] *In situ* hybridization revealed that 70% of claustral neurons expressed CaMKIIa, 26% expressed VGLUT2, and 35% of CaMKIIa-positive neurons also co-expressed VGLUT2, accounting for 24% of all claustral neurons (Figure S2). We first analyzed the population response in the ACC using the LFP evoked by optogenetic stimulation of CLA neurons. Photostimulation of CLA neurons of either population with a light pulse (5 ms duration) evoked multiphasic LFP responses in the ACC (Figures 1G and 1H). Responses were larger in the VGLUT2 population than in the CaMKIIa group both in supragranular (Figures 1I and 1J) and infragranular ACC layers (Figures 1K and 1L). Moreover, stimulation of the VGLUT2 population evoked an increase in alpha band power (8–12 Hz) in layer 2/3 that was not observed in either layer 5/6 or after broad activation of the CaMKIIa population (Figures 1I, 1K, 1M–1P, and S3). No LFP responses to photostimulation were observed in control experiments where ChR2 was not injected into the CLA (Figure S4). These results show that the activation of different subpopulations of CLA-ACC neurons induces distinct combinations of excitatory and inhibitory responses throughout the ACC.

Infragranular ACC neurons are strongly inhibited by VGLUT2 but not CaMKIIa-CLA projection neurons

The multiphasic LFP responses suggested that excitatory and inhibitory ACC neurons are dynamically and differentially affected by CLA activation. We therefore analyzed responses at the cellular level by isolating the spiking activity of multiple ACC neurons (Figure 2A). To that end, we performed spike sorting of recordings obtained from the ACC, thus recovering hundreds of well-isolated units (STAR Methods, Figure 2A; in CaMKIIa experiments, we obtained 311 units from layer 2/3 and 77 units from layer 5/6, from 35 mice. In VGLUT2 experiments, we obtained 142 units from layer 2/3 and 68 units from layer 5/6 from 21 mice). Following waveform classification, two main groups of neurons were defined: fast-spiking neurons (FS), characterized by narrow spikes (<0.5 ms) and mean firing frequency of 14.48 ± 1.14 Hz, and regular spiking (RS) neurons, characterized by wider spikes (>0.7 ms) and mean firing frequency of 5.13 ± 0.23 Hz (Figures 2B and 2C). Previous research has indicated that cortical FS neurons are primarily PV-expressing

(C) Illustration depicting experimental paradigm. Briefly, ChR2 driven by the CaMKIIa promoter (or VGLUT2-Cre) was expressed by injecting an anterograde viral vector into the CLA of different transgenic mouse lines with fluorescent reporters to identify interneuron populations. For VGLUT2-Cre mice, ChR2 was injected using an anterograde Cre-dependent virus. On the day of the recording, an optic fiber was implanted on top of the CLA.
(D) Electrophysiological recordings were performed in layer 2/3 or layer 5/6 in the ACC.
(E) Confocal image of a 250 μm experimental slice in a PV-tdTomato mouse, with a close-up in the CLA (left) and the ACC region (right) showing YFP expression in the CLA and fibers in the ipsilateral ACC but not contralateral ACC. In red, the optic fiber (left) and the silicon probe (right) are indicated.
(F) Confocal image of a 250 μm experimental slice in a VGLUT2 mouse, with a close-up in the CLA (left) and the ACC region (right) showing YFP expression in the CLA and fibers in the ipsilateral ACC but not contralateral ACC.
(G) Heatmap showing 150 repetitions of LFP responses in the ACC layer 2/3 to 5 ms photostimulation of CLA neuron subpopulations expressing CaMKIIa (left) or VGLUT2 (right).
(H) Same as in (G) but for layer 5/6.
(I) Grand average of the LFP responses in the ACC layer 2/3 to 5 ms photostimulation of CLA neurons driven by a CaMKIIa promoter (blue trace) or VGLUT2 subpopulation (red trace).
(J) The different excitations and inhibitions are marked as p1, p2, p3, and p4. $CaMKIIa_{p1}$ in 2/3 = 0.30 ± 0.08, $VGLUT2_{p1}$ in 2/3 = 1.65 ± 0.12, ***$p < 0.001$; $CaMKIIa_{p2}$ in 2/3 = −0.71 ± 0.03, $VGLUT2_{p2}$ in 2/3 = −1.81 ± 0.09, ***$p < 0.001$; $CaMKIIa_{p3}$ in 2/3 = 1.63 ± 0.21, $VGLUT2_{p3}$ in 2/3 = 2.03 ± 0.22, $p > 0.05$; $CaMKIIa_{p4}$ in 2/3 = −1.59 ± 0.04, $VGLUT2_{p4}$ in 2/3 = −1.49 ± 0.14, $p > 0.05$; two-way ANOVA test.
(K) Same as in (I) but for layer 5/6.
(L) Same as in (J) but for layer 5/6. $CaMKIIa_{p1}$ in 5/6 = 0.58 ± 0.14, $VGLUT2_{p1}$ in 5/6 = 1.67 ± 0.15, ***$p < 0.001$; $CaMKIIa_{p2}$ in 5/6 = −1.03 ± 0.09, $VGLUT2_{p2}$ in 5/6 = −1.70 ± 0.22, *$p = 0.038$; $CaMKIIa_{p3}$ in 5/6 = 1.70 ± 0.25, $VGLUT2_{p3}$ in 5/6 = 1.92 ± 0.06, $p > 0.05$; $CaMKIIa_{p4}$ in 5/6 = −1.55 ± 0.22, $VGLUT2_{p4}$ in 5/6 = −2.00 ± 0.16, $p > 0.05$; two-way ANOVA test.
(M) Power spectrum analysis of the oscillations evoked in the ACC after 5 ms photostimulation of CLA neurons driven by a CaMKIIa promoter (blue line) or VGLUT2 subpopulation (red line).
(N) Area under the curve (AUC) of the oscillations evoked in the ACC after 5 ms photostimulation of CLA neurons driven by a CaMKIIa promoter (blue line) or VGLUT2 subpopulation (red line). $CaMKIIa_{(1–4\ Hz)}$ in 2/3 = 12.96 ± 1.59, $VGLUT2_{(1–4\ Hz)}$ in 2/3 = 12.22 ± 2.22, $p > 0.05$; $CaMKIIa_{(4–8\ Hz)}$ in 2/3 = 5.92 ± 0.72, $VGLUT2_{(4–8\ Hz)}$ in 2/3 = 5.08 ± 0.74, $p > 0.05$; $CaMKIIa_{(8–12\ Hz)}$ in 2/3 = 2.95 ± 0.42, $VGLUT2_{(8–12\ Hz)}$ in 2/3 = 6.05 ± 0.17, *$p < 0.040$; $CaMKIIa_{(12–25\ Hz)}$ in 2/3 = 3.18 ± 0.31, $VGLUT2_{(12–25\ Hz)}$ in 2/3 = 11.62 ± 1.00, ***$p < 0.001$; two-way ANOVA test.
(O and P) Same as in (M) and (N) but for layer 5/6. $CaMKIIa_{(1–4\ Hz)}$ in 5/6 = 13.94 ± 2.42, $VGLUT2_{(1–4\ Hz)}$ in 5/6 = 16.30 ± 1.23, $p > 0.05$; $CaMKIIa_{(4–8\ Hz)}$ in 5/6 = 6.50 ± 1.10, $VGLUT2_{(4–8\ Hz)}$ in 5/6 = 7.77 ± 0.71, $p > 0.05$; $CaMKIIa_{(8–12\ Hz)}$ in 5/6 = 3.47 ± 0.53, $VGLUT2_{(8–12\ Hz)}$ in 5/6 = 5.17 ± 0.60, $p > 0.05$; $CaMKIIa_{(12–25\ Hz)}$ in 5/6 = 5.29 ± 0.54, $VGLUT2_{(12–25\ Hz)}$ in 5/6 = 10.12 ± 1.00, *$p = 0.023$; two-way ANOVA test.
Data are presented as mean value ± SEM. $n = 6$ mice for each group.
See also Figures S1, S2, S3, and S4.

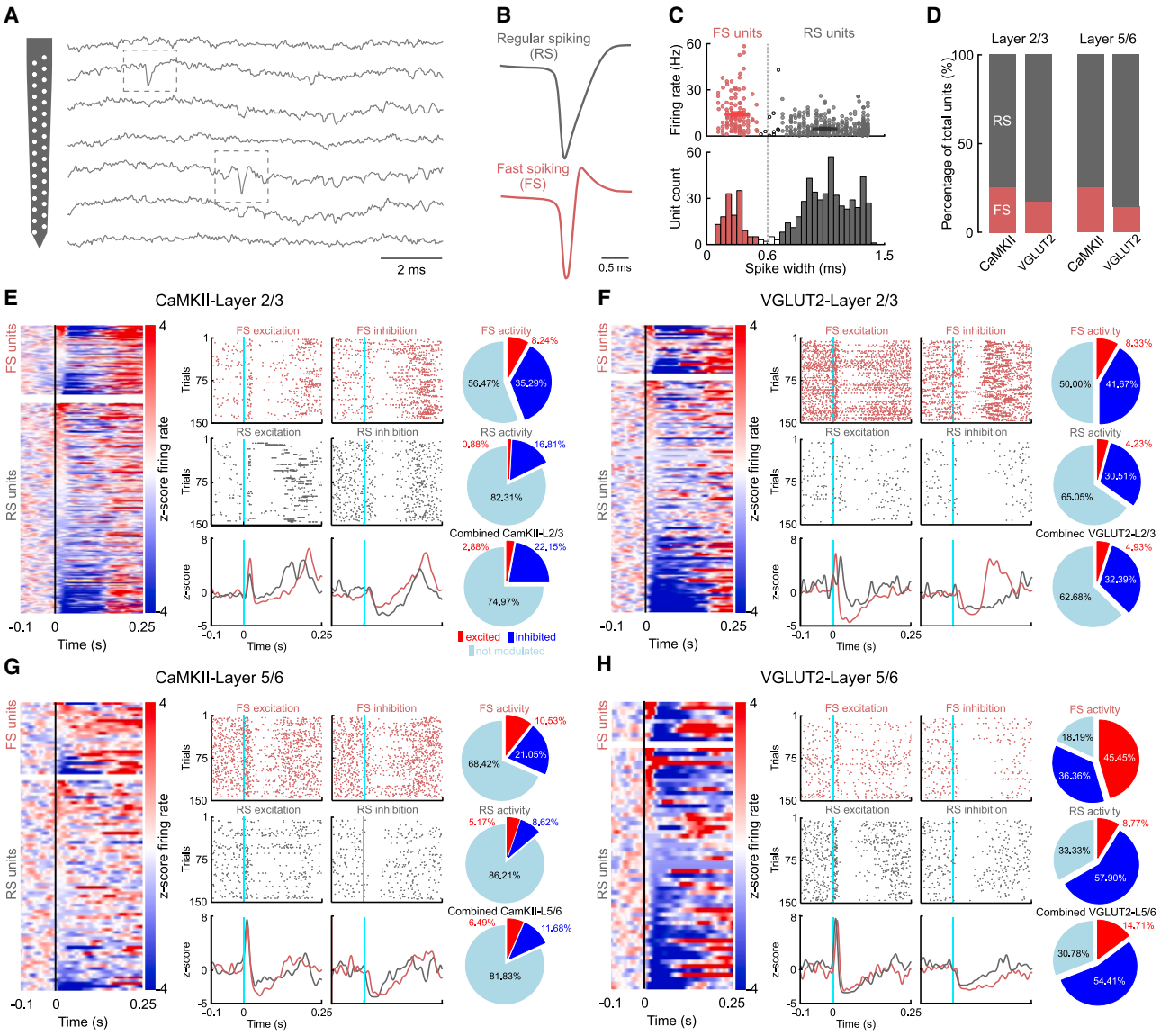

Figure 2. ACC neurons can be excited or inhibited by broad CLA neuron activation or selective VGLUT2 CLA neuron excitation

(A) Schematic of the 32-channel silicon probe (NeuroNexus A32-Poly 2). Representative *in vivo* recording performed in the mouse ACC with high-density 32-channel silicon probes.

(B) Examples of RS (gray trace) and FS (red trace) well-isolated units in the ACC.

(C) Histogram showing the distribution of the firing rate (top panel) and spike width (bottom panel) of all well-identified units in the ACC. Mean firing frequency for FS = 14.48 ± 1.14 Hz (n = 139) and for RS = 5.13 ± 0.23 Hz (n = 459; ***$p < 0.001$; Mann-Whitney test).

(D) Percentage of RS (gray bar) and FS (red bar) for each group (CaMKIIa and VGLUT2) in the different layers.

(E) Heatmap showing the responses of all well-isolated units recorded in the ACC layer 2/3 to 5 ms photostimulation of CLA neurons driven by a CaMKIIa promoter (left panel). Raster plots of example units showing excitation (middle-left panels) or inhibition (middle-right panels) for FS and RS. Proportion of RS and FS that are excited (red), inhibited (dark blue), or not modulated (light blue) in the ACC after photostimulation of the CLA neurons driven by the CaMKIIa promoter (right panels).

(F) Same as in (E) but for responses of well-isolated units recorded in the ACC layer 2/3 to 5 ms photostimulation of CLA neurons driven by the VGLUT2 promoter.

(G) Same as in (E) but for layer 5/6.

(H) Same as in (F) but for layer 5/6.

Data are presented as mean value ± SEM.

See also Figures S1–S3 and S5 and Table S1.

inhibitory interneurons, while RS neurons are likely to be a heterogeneous group that includes mostly pyramidal neurons, as well as other types of interneurons.[75]

To evaluate whether CaMKIIa and VGLUT2 CLA-ACC populations recruit FS and RS neurons to similar extents, we analyzed all the sorted single units in the ACC and their responses to CLA

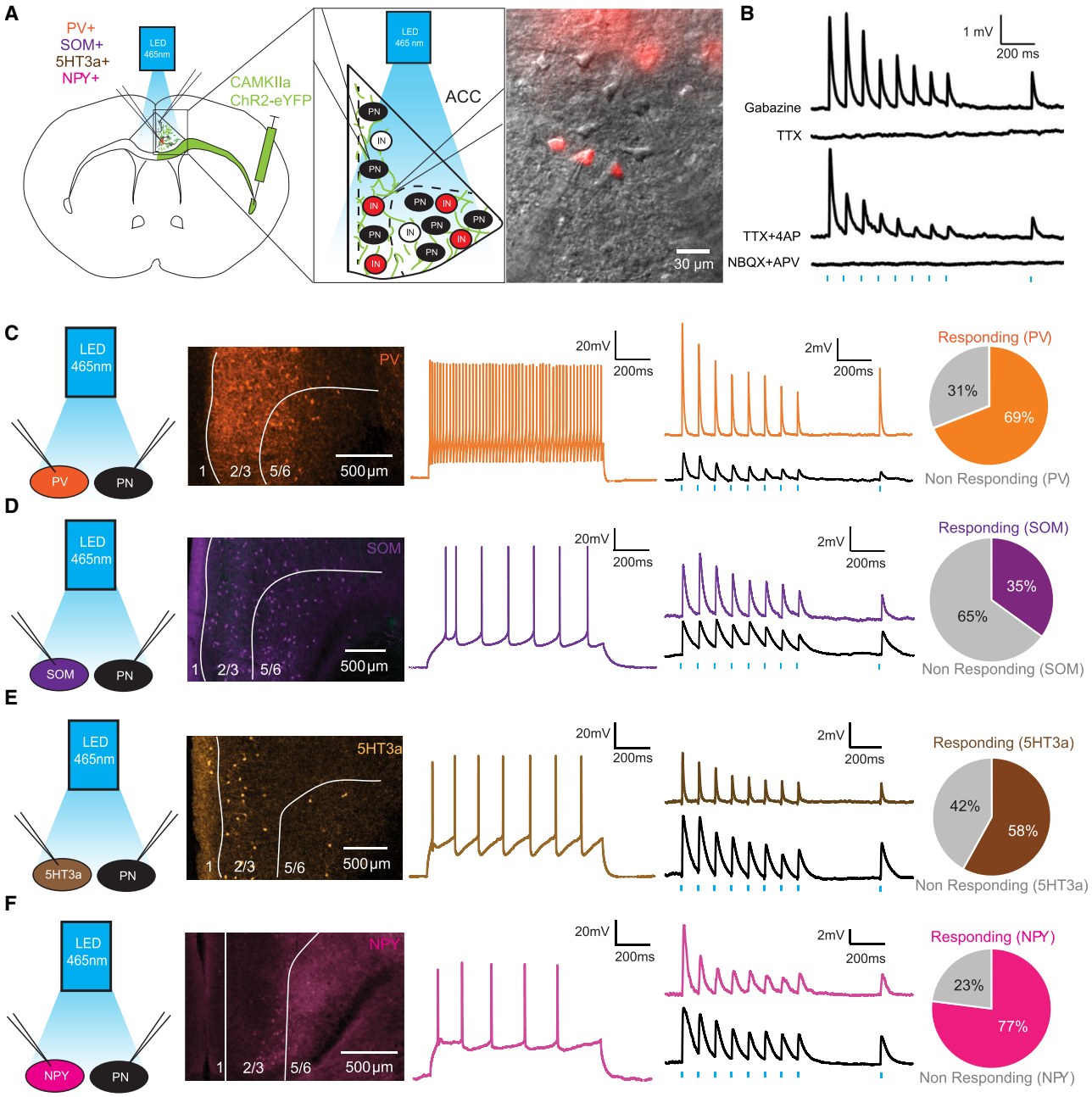

Figure 3. CLA projections selectively target interneuron populations

(A) Illustration depicting experimental paradigm. Briefly, ChR2 was injected using an anterograde viral vector into the CLA (100 nL, 300 nL/min) into different transgenic mouse lines with fluorescent reporters to identify interneuron populations. Paired whole-cell patch-clamp recordings were made in the ACC, and CLA axons were photostimulated to investigate postsynaptic responses. Differential interference contrast (DIC) image of paired recordings of an interneuron and a putative pyramidal neuron.

(B) Postsynaptic responses recorded in a layer 5/6 neuron in the presence of gabazine. The postsynaptic response was subsequently removed on bath application of TTX and recovered with TTX and 4AP, confirming that the input was monosynaptic. The subsequent postsynaptic response is abolished with AMPA and NMDA receptor antagonists, NBQX and APV, confirming that the input is excitatory.

(C) Illustration of paired recordings of PV interneurons and pyramidal neurons. Confocal image of the ACC shows that PV interneurons are in layers 2/3 and 5/6 of the ACC. A total of 75 PV interneurons (n = 42 in layer 2/3, n = 33 in layer 5/6) were studied. Example trace of a PV interneuron. Representative postsynaptic responses in paired recordings between PV (orange trace) and pyramidal neuron populations (black trace). 69% of all recorded PV neurons were found to be responsive.

(D) SOM: confocal image of the ACC shows that SOM interneurons are in layers 2/3 and 5/6 with neurites in layer 1. A total of 48 SOM interneurons (n = 1 in layer 1, n = 14 in layer 2/3, n = 33 in layer 5/6) were studied. Example trace of a SOM interneuron. Representative postsynaptic responses in paired recordings between SOM (purple trace) and pyramidal neuron populations (black trace). 35% of all recorded SOM neurons were found to be responsive.

(legend continued on next page)

photostimulation (the first 30 ms after a 5 ms light pulse). The majority of units under all conditions were RS (76% on average, Figures 2C and 2D). The modulation of ACC units was diverse, with excitatory and inhibitory responses observed in both RS and FS units (Figures 2E–2H). In layer 2/3, activation of CLA-CaMKIIa neurons excited a small fraction of FS units, while most other units were either inhibited or not affected (Figure 2E; Table S1). Photostimulation of the CLA-VGLUT2 population resulted in a similar pattern, with a minority of excited units and a large fraction of inhibited or unaffected units (Figure 2F; Table S1). Thus, activation of either CaMKIIa or VGLUT2 CLA neurons induces an overall suppression of neuronal activity in superficial ACC layers. In layer 5/6, photostimulation of CaMKIIa-expressing CLA neurons evoked a similar response as in layer 2/3, with most (82%) recorded units unaffected and the rest inhibited (12%) or excited (6%, Figure 2G; Table S1). By sharp contrast, stimulation of the CLA-VGLUT2 population evoked responses in a majority of layer 5/6 ACC units, with FS units mainly excited and RS units inhibited (Figure 2H; Table S1). The dominant feature in ACC modulation following CLA optogenetic stimulation is inhibition, as reflected by decreases in the firing rates of recorded units (Figures S5A–S5C). One exception is the infragranular FS population, which had a positive modulation index for both VGLUT2 and CaMKIIa stimulation when considering a narrower temporal window of 30 ms following stimulation (Figure S5D).

Taken together, our data show that activation of CLA neurons results in a complex pattern of inhibition and excitation of ACC neurons that depends on the presynaptic CLA projection population, the receiving ACC layer, and cortical cell type.

CLA provides excitatory monosynaptic input to ACC pyramidal neurons and interneurons

To understand the synaptic organization underlying the above *in vivo* response patterns, we obtained whole-cell patch-clamp recordings from identified pyramidal neurons and GABAergic interneurons and optogenetically stimulated CLA-ACC synaptic terminals (STAR Methods, Figure 3). In a subset of experiments, interneurons were patched simultaneously with a neighboring pyramidal neuron, enabling a direct comparison of synaptic responses under identical experimental conditions.

As in *in vivo* experiments, anterograde ChR2 virus driven by a CaMKIIa promoter was injected into the CLA in different transgenic mouse lines, and cortical slices were prepared at least 21 days after viral injection (Figures 3A and S6A). To prevent feedforward inhibitory activity,[57] the $GABA_A$ receptor blocker gabazine (10 μM) was included in the bath solution. A subset of light-responsive neurons was tested to confirm that the responses were monosynaptic by bath application of tetrodotoxin (TTX, 1 μM) followed by application of 4-aminopyridine (4-AP, 100 μM; Figures 3B and S6B).[76] Postsynaptic responses were also abolished after bath application of the glutamatergic synaptic blockers APV and NBQX (Figures 3B and S6B), indicating that responses were monosynaptic and excitatory. Neurons were filled with neurobiotin during recordings, stained, and compared post hoc with the Allen Institute Reference Atlas[77] to verify the cortical laminar position (Figure S6C).

Three main populations account for the majority of GABAergic interneurons in the cortex: PV, SOM, and 5HT3a-expressing interneurons.[67,78] PV interneurons facilitate feedforward inhibition[71] and control of excitatory and inhibitory balance within the cortex.[68,69] SOM interneurons receive facilitating excitation from cortical pyramidal neurons, target the dendrites of pyramidal neurons, and suppress the activity of other interneurons.[72] 5HT3a neurons receive thalamocortical input and mainly inhibit superficial layers of the cortex.[70] NPY interneurons constitute a population with reported overlap with both 5HT3a and SOM interneurons[70,78–80] and were previously suggested to play an important role in claustro-cortical feedforward inhibition.[57] All interneuron classes received CLA input, albeit with different probabilities. Most PV interneurons (69%, n = 52/75, Figure 3C), about one-third of SOM interneurons (35%, n = 17/48, Figure 3D), most 5HT3a interneurons (58%, n = 36/62, Figure 3E), and a large majority of NPY interneurons (77%, n = 51/66, Figure 3F) received CLA input. The majority of ACC pyramidal neurons also responded to photostimulation of CLA terminals (66%, n = 182/275).

In summary, we found that the CLA provides monosynaptic excitatory input to all tested neuron classes in the ipsilateral ACC, including pyramidal neurons and molecularly defined interneuron types.

CLA projections to different ACC interneurons display distinct connectivity profiles

While the CLA provides widespread excitatory input to the ACC, the functional impact of this connectivity depends on the specific laminar distribution and synaptic properties of these projections. We, therefore, characterized CLA-ACC synaptic responses to different neuron types according to their laminar position within the ACC. We used paired whole-cell recordings to record synaptic responses in molecularly identified interneurons and neighboring pyramidal neurons in different layers of the ACC. While similar proportions of PV interneurons in ACC layers 2/3 and 5/6 received CLA input (Figure 4A), differences were seen in the properties of their excitatory postsynaptic potentials (EPSPs) in response to CLA axon photostimulation (Figure 4B). In addition to the amplitudes of EPSPs, we also analyzed their rising slopes, as they reflect differences in the somato-dendritic position of activated synapses. PV interneurons in layer 2/3 had similar EPSP rising slopes compared with pyramidal neurons in

(E) 5HT3a: confocal image of the ACC shows that 5HT3a interneurons are located mostly in layers 1 and 2/3 with sparse labeling in layer 5/6. A total of 62 5HT3a interneurons (n = 19 in layer 1, n = 27 in layer 2/3, n = 16 in layer 5/6) were studied. Example trace from a 5HT3a interneuron. Representative postsynaptic responses in paired recordings between 5HT3a (brown trace) and pyramidal neuron populations (black trace). 58% of all recorded 5HT3a neurons were found to be responsive.

(F) NPY: confocal image of the ACC shows that NPY interneurons are in layers 1 and 2/3 with heavy labeling in layer 5/6. A total of 66 NPY interneurons (n = 10 in layer 1, n = 27 in layer 2/3, n = 29 in layer 5/6) were studied. Example trace from an NPY interneuron. Representative postsynaptic responses between NPY (magenta trace) and pyramidal neuron populations (black trace). 77% of all recorded NPY neurons were found to be responsive.

See also Figures S1, S2, S6, and S8.

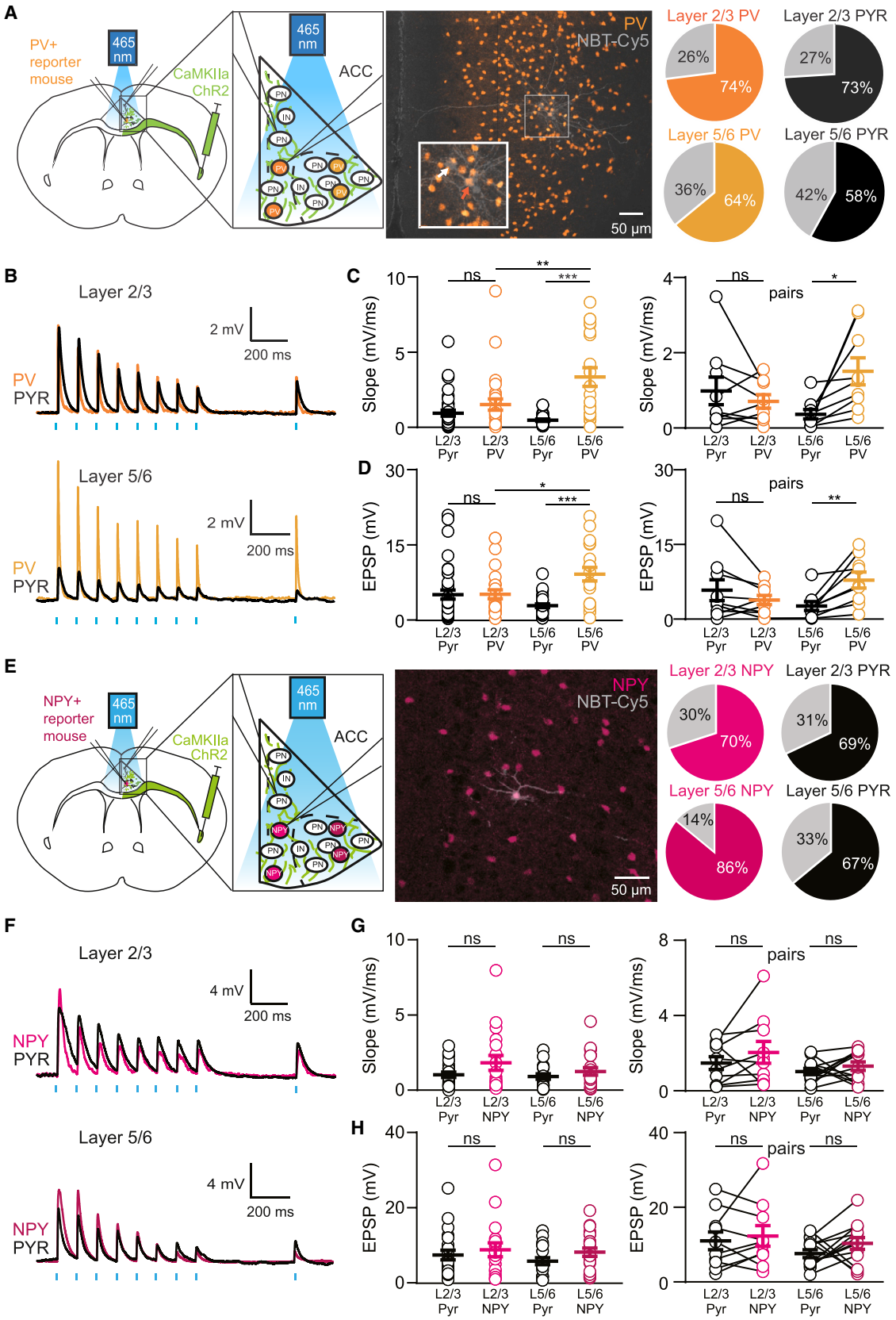

(legend on next page)

the same layer but larger rising slopes in layer 5/6 (Figure 4C). In the same line, EPSP amplitudes in layer 2/3 PV interneurons were not significantly different from amplitudes in pyramidal neurons but had significantly larger amplitudes in layer 5/6 (Figure 4D). In summary, CLA targets PV interneurons in both supra- and infragranular layers of the ACC; however, responses are stronger in infragranular PV interneurons.

To determine whether this laminar specificity extended to other interneuron populations, we next examined CLA-evoked responses in NPY-expressing interneurons. A large proportion of NPY interneurons responded to photostimulation of CLA projections in both infragranular and supragranular ACC layers (Figures 4E and 4F), including layer 1 (Figures S7A and S7B). NPY interneurons responded to CLA input with similar EPSP slopes and amplitudes as neighboring pyramidal neurons (Figures 4G and 4H).

While PV and NPY interneurons in both supra- and infragranular layers of the ACC receive robust CLA input, a different profile was observed in 5HT3a interneurons. Both layer 2/3 and layer 5/6 5HT3a interneurons received CLA input, although, in contrast with PV and NPY interneurons, there was a clear preference of layer 2/3, with only 13% (n = 2/16) of 5HT3a interneurons in layer 5/6 responding to photostimulation (Figures 5A and 5B). In addition, 5HT3a neurons in layer 1 also responded to CLA photostimulation (Figures S7A and S7B). Simultaneous recordings of neighboring 5HT3a interneurons and pyramidal neurons in ACC layer 2/3 confirmed that both cell types responded to CLA-ACC photostimulation with comparable EPSP slopes and amplitudes (Figures 5C and 5D, right).

A distinct pattern of input was identified when we analyzed the projections from CLA to SOM interneurons. Photostimulation of CLA-ACC terminals evoked robust responses in SOM interneurons primarily in infragranular ACC layers (Figures 5E and 5F), with SOM interneurons and pyramidal neurons sharing similar EPSP slopes and amplitudes (Figures 5G and 5H). In layer 2/3, only 1 out of 14 (7%) SOM interneurons responded to photostimulation, compared with 67% (n = 8/12) of pyramidal neurons under the same conditions (Figure 5E). Our data show that the CLA provides only sparse inputs to superficial SOM interneurons and preferentially targets SOM interneurons in the infragranular ACC.

In conclusion, although the CLA provides direct monosynaptic input to all neuron types tested in the ACC, the connection probability and relative amplitudes depend on both the postsynaptic neuron type and the cortical layer.

VGLUT2-expressing CLA-ACC neurons selectively target supragranular pyramidal neurons

Recent studies suggest that VGLUT2 is a selective marker for CLA projection neurons.[50,81] To investigate how this specific CLA projection population targets the ACC, Cre-dependent ChR2 virus was injected into the CLA region, and red retrograde fluorescent beads were injected into the ACC of VGLUT2-Cre transgenic mice (Figure 6A; STAR Methods). Fluorescent ChR2 fibers were observed in the ipsilateral ACC, and retrobeads were observed in VGLUT2-expressing CLA neurons (RetroBead+/VGLUT2+, Figure 6A) as well as in neurons that did not express VGLUT2 (RetroBead+/VGLUT2−, Figure 6A), suggesting that

Figure 4. CLA inputs evoke layer-dependent activation in PV interneurons, while NPY interneurons respond similarly across layers in the ACC

(A) Illustration of the experimental paradigm: simultaneous whole-cell patch-clamp recordings were made from neighboring PV interneurons and pyramidal neurons and subsequently photostimulated at 10 Hz. 74% (31/42 neurons) of PV neurons and 73% (41/56 neurons) of pyramidal neurons recorded in layer 2/3 responded to photostimulation. 64% (21/33 neurons) of PV neurons and 58% (33/57 neurons) of pyramidal neurons recorded in layer 5/6 responded to photostimulation.

(B) Representative EPSP traces from simultaneously recorded neighboring PV and pyramidal neurons in response to stimulation of CLA projections (dark orange: layer 2/3 PV; light orange: layer 5/6 PV; black: pyramidal neurons) at a frequency of 10 Hz.

(C) The activation of CaMKIIa-CLA neurons produced steeper depolarization in layer 5/6 PV interneurons compared with layer 2/3 PV interneurons (layer 2/3, PV: 1.52 ± 0.37 mV/ms; layer 5/6, PV: 3.35 ± 0.62 mV/ms; $^{**}p < 0.002$, two-way ANOVA test) and pyramidal neurons (layer 5/6 Pyr: 0.48 ± 0.07 mV/ms vs. PV: 3.35 ± 0.62 mV/ms; $^{***}p < 0.001$, two-way ANOVA test) at the population level. This result was confirmed in simultaneously recorded neighboring PV and pyramidal neurons (layer 5/6 Pyr: 0.36 ± 0.12 mV/ms vs. PV: 1.50 ± 0.36 mV/ms; $^{*}p = 0.016$, paired t test). In layer 2/3, no differences were observed when comparing PV and pyramidal neurons (Pyr: 0.95 ± 0.19 mV/ms vs. PV: 1.52 ± 0.37 mV/ms; $p > 0.05$, two-way ANOVA test) either at the population level or in simultaneously recorded neurons (Pyr: 0.98 ± 0.37 mV/ms vs. PV: 0.70 ± 0.18 mV/ms; $p > 0.05$, paired t test).

(D) The activation of CaMKIIa-CLA neurons produced larger EPSPs in layer 5/6 PV interneurons compared with layer 2/3 PV interneurons (layer 2/3 PV: 5.10 ± 0.88 mV/ms, layer 5/6 PV: 9.12 ± 1.34 mV/ms; $^{*}p < 0.023$, two-way ANOVA test) and pyramidal neurons (layer 5/6 Pyr: 2.81 ± 0.38 mV/ms vs. $PV_{L5/6}$: 9.12 ± 1.34 mV/ms; $^{***}p < 0.001$, two-way ANOVA test) at the population level. This result was confirmed in simultaneously recorded neighboring PV and pyramidal neurons (layer 2/3, Pyr: 5.84 ± 2.08 mV vs. PV: 3.87 ± 0.92 mV; $p > 0.05$; layer 5/6 Pyr: 2.68 ± 0.87 mV vs. PV: 7.85 ± 1.58 mV; $^{**}p = 0.005$, paired t test).

(E) Illustration of the experimental paradigm in NPY+ reporter mice. 70% (19/27 neurons) of NPY neurons and 69% (24/35 neurons) of pyramidal neurons recorded in layer 2/3 responded to photostimulation. 86% (25/29 neurons) of NPY neurons and 67% (20/31 neurons) of pyramidal neurons recorded in layer 5/6 responded to photostimulation.

(F) Representative EPSP traces from simultaneously recorded neighboring NPY and pyramidal neurons in response to stimulation of CLA projections (light pink: layer 2/3 NPY; dark pink: layer 5/6 NPY; black: pyramidal neurons) at a frequency of 10 Hz.

(G) The activation of CaMKIIa-CLA neurons depolarized NPY and pyramidal neurons in layer 2/3 and 5/6, with no significant differences in the depolarization speed, as indicated by the slope at the population level (layer 2/3, Pyr: 1.04 ± 0.18 mV/ms, NPY: 1.84 ± 0.49 mV/ms; $p > 0.05$; layer 5/6, Pyr: 0.93 ± 0.18 mV/ms, NPY: 1.27 ± 0.25 mV/ms, $p > 0.05$, two-way ANOVA test). This result was confirmed in simultaneously recorded neighboring NPY and pyramidal neurons (layer 2/3, Pyr: 1.45 ± 0.34 mV/ms, NPY: 2.02 ± 0.58 mV/ms, $p > 0.05$, paired t test; layer 5/6, Pyr: 1.00 ± 0.17 mV/ms, NPY: 1.29 ± 0.22 mV/ms, $p > 0.05$, paired t test).

(H) The activation of CaMKIIa-CLA neurons depolarized NPY and pyramidal neurons in layer 2/3 and 5/6, with no significant difference in the EPSP amplitude between neurons at the population level (layer 2/3, Pyr: 7.47 ± 1.26 mV, NPY: 8.85 ± 1.83 mV, $p > 0.05$, two-way ANOVA test; layer 5/6, Pyr: 5.81 ± 0.93 mV, NPY: 8.23 ± 1.10 mV, $p > 0.05$, two-way ANOVA test). This result was confirmed in simultaneously recorded neighboring NPY and pyramidal neurons (layer 2/3, Pyr: 11.07 ± 2.38 mV, NPY: 12.37 ± 2.74 mV, $p > 0.05$, paired t test; layer 5/6, Pyr: 7.65 ± 1.05 mV, NPY: 10.37 ± 1.55 mV, $p > 0.05$, paired t test).

Data are presented as mean value ± SEM.

See also Figures S1, S7, and S8.

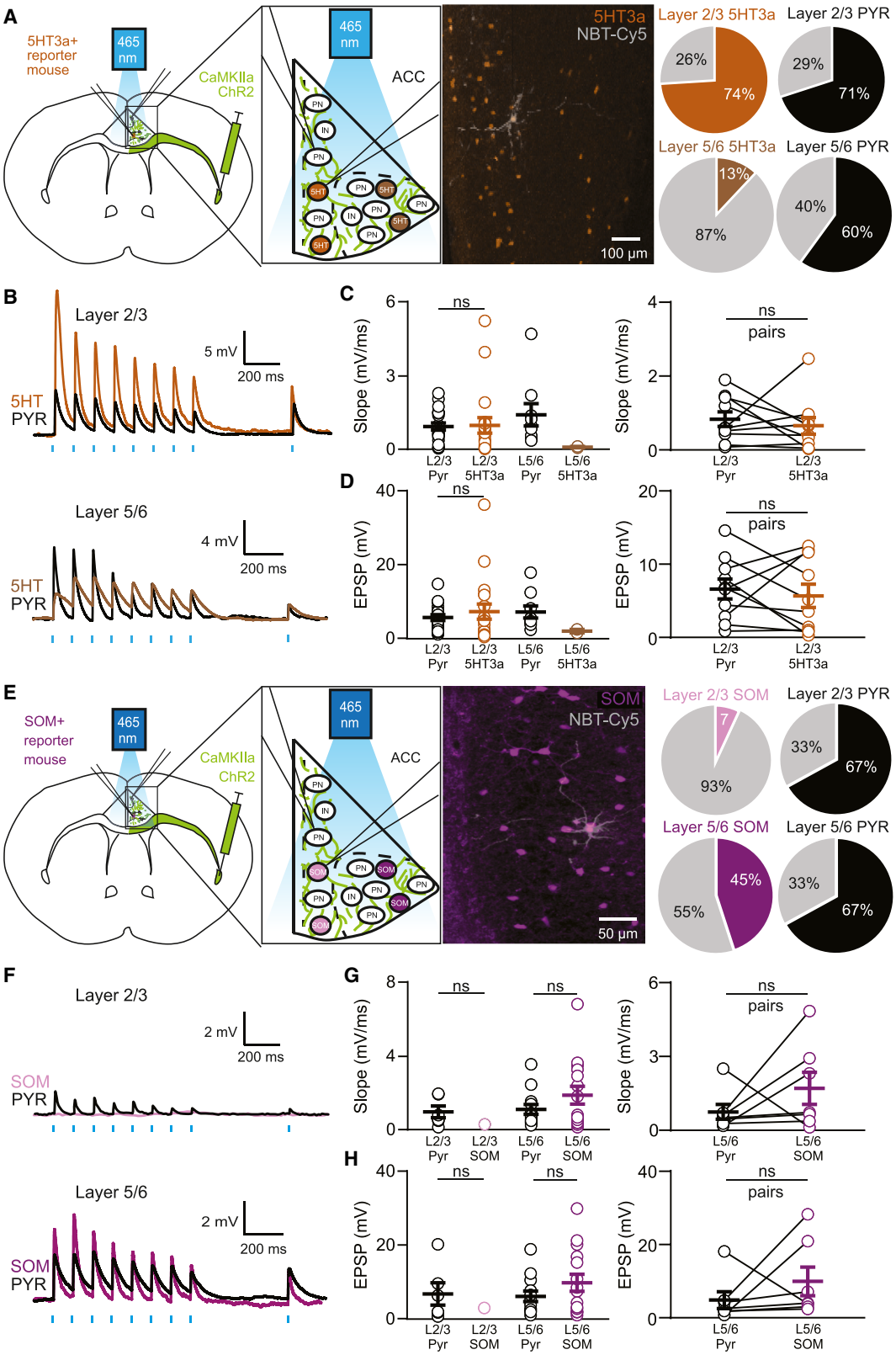

(legend on next page)

the CLA-ACC pathway is mediated by both VGLUT2-positive and negative projection neurons. *Ex vivo* whole-cell patch-clamp recordings were performed from neurons in the ACC of VGLUT2-Cre mice infected with Cre-dependent ChR2 virus in CLA. In these experiments, FS interneurons (putative PV expressing) and pyramidal neurons were classified based on their morphological and electrophysiological properties (Figures 6B, 6E, and S8).

In layer 2/3, most pyramidal neurons responded to photostimulation of CLA-VGLUT2 axons (82%, n = 28/34) compared with FS interneurons (55%, n = 5/9) (Figures 6B–6D). Markedly, the opposite was observed in infragranular ACC, with only a minority of pyramidal neurons (29%, n = 15/51 neurons) but nearly all FS interneurons (89%, n = 8/9) in layer 5/6 responding to photostimulation (Figures 6E–6G). EPSPs in both pyramidal neurons and FS interneurons were attenuated in the presence of TTX (1 μM) and recovered following the administration of 4AP (100 μM, Figure 6H), showing that VGLUT2-expressing neurons establish monosynaptic connections onto both populations. In layer 5/6, EPSP slopes in infragranular FS interneurons were larger than those in neighboring pyramidal neurons (Figure 6I). We also found that all neurons (undefined type) in layer 1 responded to photostimulation of CLA-VGLUT2 terminals (n = 6/6, Figure S7E). In summary, these data show that CLA-VGLUT2 projection neurons primarily target pyramidal neurons in supragranular layers of the ACC while providing robust and fast excitation to infragranular FS interneurons.

Taken together, our data reveal a high degree of specificity and intricate organization of the CLA-ACC pathway, involving different populations of CLA neurons, recipient cortical layers, and cortical neuron classes. While all tested ACC neuron types received input from CLA, the connection probabilities and strengths varied significantly, thus forming the circuit substrate for complex dynamic interactions between these two structures.

DISCUSSION

In this study, we used a combination of *in vivo* and *ex vivo* electrophysiology to reveal the organizing principles, targets, and influence of CLA projections to the ACC. We show that *in vivo* activation of CLA neurons produces a combination of excitation and inhibition that depends on three factors: the identity of the projecting CLA neuron, the targeted ACC layer, and the type of postsynaptic neuron in ACC. Using *ex vivo* paired whole-cell recordings, we obtained a detailed mapping of the pathway revealing that excitatory monosynaptic CLA projections to ACC targeted PV and NPY interneurons in both layers 2/3 and 5/6, while preferentially targeting 5HT3a interneurons in the supragranular layers and SOM interneurons in the infragranular layers. This intricate synaptic organization of the CLA-ACC pathway underlies the complex dynamics seen in ACC following CLA activation and may explain the variability in cortical responses observed in previous studies.

Modulation of ACC by broad activation of CLA neurons *in vivo*

The CLA has been reported to exert either excitatory or inhibitory effects on different cortical regions.[1,18,50,57] Our data and previous studies provide evidence showing that CLA neurons target both excitatory and inhibitory neurons within cortical circuits.[2,10,57] In addition, the fact that CLA is composed of different neuron types indicates that simultaneous activation of all projection neurons may account for the discrepancy observed regarding the influence of CLA on cortical processing.[11,12,19] Our *in vivo* LFP recordings show that broad optogenetic activation of CLA neurons expressing ChR2 driven by the CaMKIIa promoter evokes brief excitation followed by pronounced inhibition in the ACC. This type of response was observed both in layer 2/3 and layer 5/6 and suggests, as previously reported,[18,27,57] that CLA provides a "blanket of inhibition" to the ACC. However, LFP recordings have proven notoriously difficult to interpret,[82–84]

Figure 5. CLA projections preferentially target 5HT3a interneurons in superficial layers and SOM interneurons in deep layers

(A) Illustration of the experimental paradigm in 5HT3a+ reporter mice. 74% (20/27 neurons) of 5HT3a neurons and 71% (22/31 neurons) of pyramidal neurons recorded in layer 2/3 responded to photostimulation. 13% (2/16 neurons) of 5HT3a neurons and 60% (9/15 neurons) of pyramidal neurons recorded in layer 5/6 responded to photostimulation.

(B) Representative EPSP traces from simultaneously recorded neighboring 5HT3a and pyramidal neurons in response to stimulation of CLA projections (light brown: layer 2/3 5HT3a; dark brown: layer 5/6 5HT3a; black: pyramidal neurons) at a frequency of 10 Hz.

(C) The activation of CaMKIIa-CLA neurons depolarized 5HT3a and pyramidal neurons in layer 2/3 with no significant differences in the depolarization speed, as indicated by the slope at the population level (Pyr: 0.93 ± 0.15 mV/ms, 5HT3a: 0.98 ± 0.31 mV/ms; $p > 0.05$, two-way ANOVA test). This result was confirmed in simultaneously recorded neighboring 5HT3a and pyramidal neurons (Pyr: 0.84 ± 0.19 mV/ms, 5HT3a: 0.66 ± 0.23 mV/ms; $p > 0.05$, paired t test).

(D) The activation of CaMKIIa-CLA neurons depolarized 5HT3a and pyramidal neurons in layer 2/3 with no significant difference in the EPSP amplitude between neurons at the population level (Pyr: 5.66 ± 0.79 mV, 5HT3a: 7.26 ± 2.04 mV; $p > 0.05$, two-way ANOVA test). This result was confirmed in simultaneously recorded neighboring 5HT3a and pyramidal neurons (Pyr: 6.55 ± 1.35 mV, 5HT3a: 5.61 ± 1.57 mV, $p > 0.05$, paired t test).

(E) Illustration of the experimental paradigm in SOM+ reporter mice. 7% (1/14 neurons) of SOM neurons and 67% (8/12 neurons) of pyramidal neurons recorded in layer 2/3 responded to photostimulation, while 45% (15/33 neurons) of SOM neurons and 67% (14/21 neurons) of pyramidal neurons recorded in layer 5/6 responded to photostimulation.

(F) Representative EPSP traces from simultaneously recorded neighboring SOM and pyramidal neurons in response to stimulation of CLA projections (light purple: layer 2/3 SOM; dark purple: layer 5/6 SOM; black: pyramidal neurons) at a frequency of 10 Hz.

(G) The activation of CaMKIIa-CLA neurons depolarized SOM and pyramidal neurons in layer 5/6 with no significant differences in the depolarization speed, as indicated by the slope at the population level (Pyr: 1.09 ± 0.26 mV/ms, SOM: 1.86 ± 0.48 mV/ms; $p > 0.05$, two-way ANOVA test). This result was confirmed in simultaneously recorded neighboring SOM and pyramidal neurons (Pyr: 0.76 ± 0.30 mV/ms, SOM: 1.72 ± 0.66 mV/ms; $p > 0.05$, paired t test).

(H) The activation of CaMKIIa-CLA neurons depolarized SOM and pyramidal neurons in layer 5/6 with no significant difference in the EPSP amplitude between neurons at the population level (Pyr: 6.11 ± 1.43 mV, SOM: 9.81 ± 2.31 mV; $p > 0.05$, two-way ANOVA test). This result was confirmed in simultaneously recorded neighboring SOM and pyramidal neurons (Pyr: 4.96 ± 2.26 mV, SOM: 10.02 ± 3.88 mV; $p > 0.05$, paired t test).

Data are presented as mean value ± SEM.

See also Figures S1, S7, and S8.

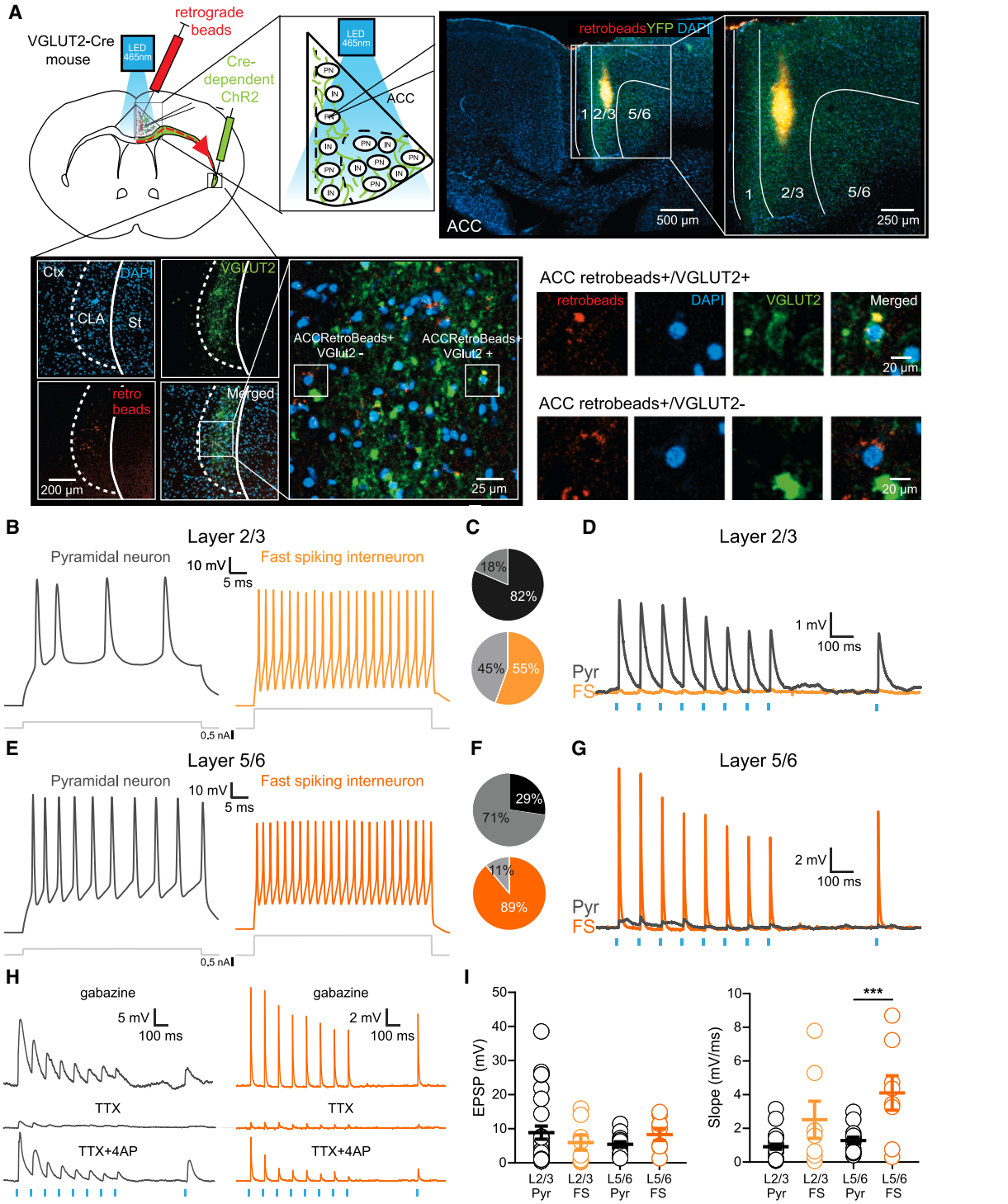

Figure 6. VGLUT2-expressing CLA neurons selectively target pyramidal neurons in the superficial ACC layers while targeting FS neurons in the deeper layers

(A) Top left: illustration of the experimental paradigm. Retrograde fluorescent beads were injected into the ACC, and Cre-dependent ChR2 virus was injected into the CLA of VGLUT2-Cre transgenic mice. Whole-cell patch-clamp recordings were made in all layers of the ACC and CLA axons were subsequently photo-stimulated at 10 Hz. Top right: Confocal image of a 250 µm experimental slice, showing injection of red retrograde beads into the ACC and CLA axons expressing YFP in the ACC. Bottom left: confocal image of the same 250 µm experimental slice showing VGLUT2 expression and CLA-ACC neurons in the CLA. Bottom right: examples of retrogradely labeled CLA-ACC neurons expressing (top row, VGLUT2+) and not expressing VGLUT2 (bottom row, VGLUT2−).

(B) A putative pyramidal neuron in ACC layer 2/3 (left, gray trace) showed a broader action potential with a relatively longer spike width compared with an FS neuron (putative Pv interneuron, right, orange trace).

(legend continued on next page)

and our analysis of unit recordings showed that CLA photostimulation triggered a combination of excitation and inhibition in the ACC. In this context, although FS units were more likely to be excited than RS ones, we also observed excitation of RS units, mainly in deep layers (Figures 2G, 2H, and 2J). On the other hand, the proportion of both RS and FS units inhibited after photostimulation of CLA neurons was larger than the excited units, especially in supragranular layers (Figure 2J). This inhibition is weaker than the near-total and prolonged silence of cortical neurons reported previously.[27,57] The response of ACC neurons to optogenetic activation of CLA projection neurons was often multiphasic, consisting of an early and brief increase in firing rate, followed by a delayed and longer inhibition (Figure 2). These complex responses at different timescales (Figure S5) reflect the cortical polysynaptic cascades activated by CLA excitation.

Regarding different presynaptic CLA subpopulations, it has been shown that activation of a subpopulation of Esr2-expressing CLA neurons evoked only a moderate inhibitory effect despite their preference for FS and little impact in RS.[18] This raises the possibility that Esr2-expressing neurons may express their own target selectivity in the cortex. Recent studies have described that specific subsets of CLA neurons, particularly those expressing VGLUT2, can elicit a net excitatory effect in the cortex,[50] contradicting previous claims of a widespread inhibitory influence.[18,27,57] We observed comparable proportions of excitation and inhibition in layer 2/3 of VGLUT2 and CaMKIIa mice. By contrast, activation of VGLUT2 CLA neurons led to a substantial recruitment of layer 5/6 FS neurons (Figures 2H and 2J). This robust recruitment of layer 5/6 FS neurons coincided with a pronounced inhibition of RS neurons, surpassing the level observed in CaMKIIa mice. These data suggest that although the innervation of VGLUT2 CLA-ACC terminals is denser in supragranular layers, it still excites infragranular ACC neurons, with a target preference of GABAergic interneurons accounting for the overall inhibitory response.

Selective targeting of ACC interneurons by CLA projections

Our data show marked differences in the CLA targeting of interneurons according to their type and laminar distribution. This innervation pattern is likely to contribute to the complex excitation/inhibition patterns observed in our study (Figures 1 and 2) and others.[18,27,50,57] Our results show that CLA projection neurons preferentially targeted PV interneurons in both supra- and infragranular layers, 5HT3a interneurons in the supragranular layers, and SOM interneurons in the infragranular layers. They also targeted NPY interneurons, which were suggested to play a crucial role in claustro-cortical feedforward inhibition.[57] The different types of cortical interneurons have distinct target preferences, providing inhibition to both excitatory and inhibitory cortical neurons.[65,85–87] Specifically, it has been shown that NPY interneurons in the prefrontal cortex activated by CLA neurons provide feedforward inhibition to both pyramidal neurons and PV interneurons.[57] In addition to the selective targeting of interneurons in layers 2/3 vs. 5/6, we show that 5HT3a and NPY interneurons in layer 1 also received CLA input. Layer 1 receives input from brain regions associated with higher cognitive functions as well as specific neuromodulatory inputs.[76,88–93] These inputs modulate the activity of the entire cortical column[94] via complex local inhibitory and disinhibitory circuits.[90,92] All of the above excitatory, inhibitory, and disinhibitory pathways control the firing of cortical neurons in different cortical layers, as seen in extracellular *in vivo* recordings.[18,50,57] In agreement with anatomical data reported in recent studies,[50] our data show that VGLUT2-expressing CLA projection neurons preferentially target pyramidal neurons in layer 2/3 of the ACC. We also show that the VGLUT2-expressing CLA neurons preferentially target PV interneurons in layer 5/6, which is in line with the observed excitation in FS neurons *in vivo* (Figure 2H). The differences between CaMKIIa and VGLUT2 projection neurons may not only help explain discrepancies in the literature regarding the impact of CLA on cortical activity but also shed light on processes such as pain perception. For instance, recent publications have reported that activation of CLA neurons in inflammatory pain models in mice produces analgesia and attenuates the sensation of pain.[46] Conversely, a different study indicates that the same inflammatory model does not alter CLA function.[37] Our findings provide a framework that may explain this discrepancy, as the different CLA subpopulations have distinct connectivity patterns with cortex.

Strengths and limitations of the study and future directions

We used fluorescent markers for several GABAergic interneuron populations, which were simultaneously recorded with

(C) Most putative pyramidal neurons in ACC layer 2/3 responded to photostimulation of VGLUT2 CLA-ACC terminals (82%, $n = 28/34$), whereas only half of the FS neurons responded to the same stimulation (55%, $n = 5/9$).
(D) Representative traces of EPSPs produced in an FS and a pyramidal neuron in response to stimulation of VGLUT2-CLA projections (light orange: layer 2/3 FS; black: pyramidal neuron) at a frequency of 10 Hz.
(E) Same as in (B) but for layer 5/6.
(F) Only a small minority (29%, $n = 15/51$) of ACC layer 5/6 pyramidal neurons responded to VGLUT2 CLA-ACC photostimulation, compared with a majority in superficial layers (82%, $n = 28/34$, $p < 0.001$, chi-squared test). By contrast, nearly all recorded FS neurons responded to the stimulation (100%, $n = 8/9$, layer 5/6: Pyr vs. FS, $p < 0.002$, chi-squared test).
(G) Representative EPSP traces of an FS and a pyramidal neuron in response to stimulation of VGLUT2-CLA projections (dark orange: layer 5/6 FS; black: pyramidal neuron) at a frequency of 10 Hz.
(H) Synaptic responses were attenuated in both pyramidal and FS neurons by TTX and recovered following application of 4AP.
(I) EPSP rising slopes and amplitudes in response to photostimulation of VGLUT2 CLA-ACC terminals across different ACC layers. No significant differences in EPSP amplitude were observed between layers in either pyramidal neurons or FS neurons (layer 2/3: Pyr: 8.80 ± 1.92 mV; FS layer 2/3: 5.91 ± 2.20 mV; layer 5/6: Pyr: 5.41 ± 0.71 mV; FS layer 5/6: 8.25 ± 1.77 mV; $p > 0.5$ in all comparisons, two-way ANOVA test). Layer 5/6 FS neurons responded to VGLUT2-CLA neuron activation with a significantly faster depolarization compared with pyramidal neurons in the same layer (layer 5/6: Pyr: 1.27 ± 0.20 mV/ms, FS: 4.10 ± 1.02 mV/ms; $^{***}p < 0.001$; two-way ANOVA test).
Data are presented as mean value ± SEM.
See also Figures S2 and S7.

neighboring pyramidal neurons; however, cortical pyramidal neurons are made up of different subpopulations,[95] which were not classified here. Moreover, the molecular markers we used for GABAergic interneurons in the ACC have a certain degree of overlap, in particular the NPY population, which partially overlaps with both SOM- and 5HT3a-expressing interneurons.[70,79,80] This convergence may explain the robust responses in both supra- and infragranular NPY interneurons (Figure 4). Using paired recordings of interneurons and pyramidal neurons allowed the *ex vivo* data to be controlled for variations in animals, viral titer, incubation time, viral expression, cell type, and brain slice quality across and within experiments. To identify the various molecularly defined mouse lines, we crossed a Cre-dependent line with a tdTomato reporter. It should be noted that the VGLUT2 population constitutes a subset of the larger CaMKIIa-expressing population.[48] Further studies are required to establish the detailed targeting of cortical neurons by different CLA neuron types, such as those expressing VGLUT1, Esr2, GnB4, Erg2, Nurr1, and others.[18,48,96,97] In this paper, we built on our previous work[10,11] by using the robust CLA-ACC pathway to investigate cell-type and layer targets of CLA input at a specific cortical region. As there is a growing understanding that cortical microcircuits significantly differ across regions,[98,99] similar work should be performed on other granular and agranular cortices to create a complete canonical claustro-cortical scheme.

Conclusion

In conclusion, we report that CLA activation evokes synaptic responses in all layers of the ACC and that these responses depend on the identity of the presynaptic CLA projection, the targeted cortical layer, and the identity of the postsynaptic neuron. Our results explain some of the discrepancies regarding the excitatory or inhibitory influence of the CLA in the ACC and lay the foundation for understanding the organizing principles of claustro-cortical connectivity.

RESOURCE AVAILABILITY

Lead contact

Further information and requests for resources and reagents should be directed to and will be fulfilled by the lead contact, Gilad Silberberg (gilad.silberberg@ki.se).

Materials availability

This study did not generate new, unique reagents.

Data and code availability

All data reported in this paper will be shared by the lead contact upon request. This paper does not report original code. Any additional information required to reanalyze the data reported in this paper is available from the lead contact upon request.

ACKNOWLEDGMENTS

We thank Peter Löw for his technical support with the RNAscope experiments. We thank the Silberberg lab for helpful discussions, Sten Grillner and Abdel El Manira for comments on earlier versions, and Ainara and Erik for their continuous support. This work was funded by a Wallenberg Fellowship from the Knut and Alice Wallenberg Foundation (KAW 2017.0273), the Swedish Brain Foundation (Hjärnfonden, FO2021-0333, FO2023-0230), and the Swedish Medical Research Council (VR-M, 2023-02304) to G.S. and a Singapore Ministry of Education grant (MOE2015-T2-2-095) to G.J.A. R.d.l.T.-M. was supported by a Karolinska Institute postdoctoral scholarship and a StratNeuro postdoctoral grant. Z.C. was supported by the Nanyang Technological University – Karolinska Institutet Joint PhD Program. A.T., J.B., and J.F.-N. were supported by a Karolinska Institute doctoral grant.

AUTHOR CONTRIBUTIONS

R.d.l.T.-M. organized and performed *in vivo* experimental work, RNAscope, confocal imaging, and data analysis. Z.C. organized and performed *ex vivo* experimental work and data analysis. A.T. and J.B. performed and analyzed *ex vivo* experiments. J.F.-N. analyzed *in vivo* data. R.d.l.T.-M., Z.C., G.J.A., and G.S. were responsible for experimental design. All authors contributed to manuscript preparation.

DECLARATION OF INTERESTS

The authors declare no competing interests.

STAR★METHODS

Detailed methods are provided in the online version of this paper and include the following:

- KEY RESOURCES TABLE
- EXPERIMENTAL MODEL AND STUDY PARTICIPANT DETAILS
- METHOD DETAILS
  - Virus injection
  - Head implants
  - *In vivo* electrophysiology
  - *In vivo* photostimulation
  - Spike sorting
  - Modulation index calculations
  - Brain slice preparation
  - Whole-cell patch-clamp recordings
  - Determination of cortical layer
  - Photostimulation in brain slices
  - RNAscope *in situ* hybridization
  - Confocal imaging
- QUANTIFICATION AND STATISTICAL ANALYSIS

SUPPLEMENTAL INFORMATION

Supplemental information can be found online at https://doi.org/10.1016/j.cub.2025.05.056.

Received: December 3, 2024
Revised: May 4, 2025
Accepted: May 28, 2025
Published: June 18, 2025

REFERENCES

1. Atlan, G., Terem, A., Peretz-Rivlin, N., Groysman, M., and Citri, A. (2017). Mapping synaptic cortico-claustral connectivity in the mouse. J. Comp. Neurol. *525*, 1381–1402. https://doi.org/10.1002/cne.23997.
2. Carman, J.B., Cowan, W.M., and Powell, T.P. (1964). The Cortical Projection Upon the Claustrum. J. Neurol. Neurosurg. Psychiatry *27*, 46–51. https://doi.org/10.1136/jnnp.27.1.46.
3. Sloniewski, P., Usunoff, K.G., and Pilgrim, C. (1986). Diencephalic and mesencephalic afferents of the rat claustrum. Anat. Embryol. (Berl) *173*, 401–411. https://doi.org/10.1007/BF00318925.
4. Smith, J.B., Radhakrishnan, H., and Alloway, K.D. (2012). Rat claustrum coordinates but does not integrate somatosensory and motor cortical information. J. Neurosci. *32*, 8583–8588. https://doi.org/10.1523/JNEUROSCI.1524-12.2012.

5. Smith, J.B., and Alloway, K.D. (2010). Functional specificity of claustrum connections in the rat: interhemispheric communication between specific parts of motor cortex. J. Neurosci. *30*, 16832–16844. https://doi.org/10.1523/JNEUROSCI.4438-10.2010.

6. Wang, Q., Ng, L., Harris, J.A., Feng, D., Li, Y., Royall, J.J., Oh, S.W., Bernard, A., Sunkin, S.M., Koch, C., et al. (2017). Organization of the connections between claustrum and cortex in the mouse. J. Comp. Neurol. *525*, 1317–1346. https://doi.org/10.1002/cne.24047.

7. Zhang, X., Hannesson, D.K., Saucier, D.M., Wallace, A.E., Howland, J., and Corcoran, M.E. (2001). Susceptibility to kindling and neuronal connections of the anterior claustrum. J. Neurosci. *21*, 3674–3687. https://doi.org/10.1523/JNEUROSCI.21-10-03674.2001.

8. Zingg, B., Hintiryan, H., Gou, L., Song, M.Y., Bay, M., Bienkowski, M.S., Foster, N.N., Yamashita, S., Bowman, I., Toga, A.W., et al. (2014). Neural networks of the mouse neocortex. Cell *156*, 1096–1111. https://doi.org/10.1016/j.cell.2014.02.023.

9. Zingg, B., Dong, H.W., Tao, H.W., and Zhang, L.I. (2018). Input-output organization of the mouse claustrum. J. Comp. Neurol. *526*, 2428–2443. https://doi.org/10.1002/cne.24502.

10. Chia, Z., Silberberg, G., and Augustine, G.J. (2017). Functional properties, topological organization and sexual dimorphism of claustrum neurons projecting to anterior cingulate cortex. Claustrum *2*, 1357412. https://doi.org/10.1080/20023294.2017.1357412.

11. Chia, Z., Augustine, G.J., and Silberberg, G. (2020). Synaptic Connectivity between the Cortex and Claustrum Is Organized into Functional Modules. Curr. Biol. *30*, 2777–2790.e4. https://doi.org/10.1016/j.cub.2020.05.031.

12. da Costa, N.M., Fürsinger, D., and Martin, K.A.C. (2010). The synaptic organization of the claustral projection to the cat's visual cortex. J. Neurosci. *30*, 13166–13170. https://doi.org/10.1523/JNEUROSCI.3122-10.2010.

13. Jackson, J. (2018). Attention: Noisy Networks Are Tuned Out by the Claustrum. Curr. Biol. *28*, R937–R939. https://doi.org/10.1016/j.cub.2018.07.031.

14. Kim, J., Matney, C.J., Roth, R.H., and Brown, S.P. (2016). Synaptic Organization of the Neuronal Circuits of the Claustrum. J. Neurosci. *36*, 773–784. https://doi.org/10.1523/JNEUROSCI.3643-15.2016.

15. Li, Z.K., Takada, M., and Hattori, T. (1986). Topographic organization and collateralization of claustrocortical projections in the rat. Brain Res. Bull. *17*, 529–532. https://doi.org/10.1016/0361-9230(86)90220-0.

16. Minciacchi, D., Molinari, M., Bentivoglio, M., and Macchi, G. (1985). The organization of the ipsi- and contralateral claustrocortical system in rat with notes on the bilateral claustrocortical projections in cat. Neuroscience *16*, 557–576. https://doi.org/10.1016/0306-4522(85)90192-7.

17. Sadowski, M., Moryś, J., Jakubowska-Sadowska, K., and Narkiewicz, O. (1997). Rat's claustrum shows two main cortico-related zones. Brain Res. *756*, 147–152. https://doi.org/10.1016/s0006-8993(97)00135-2.

18. McBride, E.G., Gandhi, S.R., Kuyat, J.R., Ollerenshaw, D.R., Arkhipov, A., Koch, C., and Olsen, S.R. (2023). Influence of claustrum on cortex varies by area, layer, and cell type. Neuron *111*, 275–290.e5. https://doi.org/10.1016/j.neuron.2022.10.026.

19. Shelton, A.M., Oliver, D.K., Lazarte, I.P., Grimstvedt, J.S., Kapoor, I., Swann, J.A., Ashcroft, C.A., Williams, S.N., Conway, N., Tir, S., et al. (2024). Single neurons and networks in the claustrum integrate input from widespread cortical sources. Preprint at BioRxiv, 202205.

20. Wang, Q., Wang, Y., Kuo, H.C., Xie, P., Kuang, X., Hirokawa, K.E., Naeemi, M., Yao, S., Mallory, M., Ouellette, B., et al. (2023). Regional and cell-type-specific afferent and efferent projections of the mouse claustrum. Cell Rep. *42*, 112118. https://doi.org/10.1016/j.celrep.2023.112118.

21. Qadir, H., Stewart, B.W., VanRyzin, J.W., Wu, Q., Chen, S., Seminowicz, D.A., and Mathur, B.N. (2022). The mouse claustrum synaptically connects cortical network motifs. Cell Rep. *41*, 111860. https://doi.org/10.1016/j.celrep.2022.111860.

22. Peng, H., Xie, P., Liu, L., Kuang, X., Wang, Y., Qu, L., Gong, H., Jiang, S., Li, A., Ruan, Z., et al. (2021). Morphological diversity of single neurons in molecularly defined cell types. Nature *598*, 174–181. https://doi.org/10.1038/s41586-021-03941-1.

23. Barbier, M., Houdayer, C., Franchi, G., Poncet, F., and Risold, P.Y. (2017). Melanin-concentrating hormone axons, but not orexin or tyrosine hydroxylase axons, innervate the claustrum in the rat: An immunohistochemical study. J. Comp. Neurol. *525*, 1489–1498. https://doi.org/10.1002/cne.24110.

24. Barbier, M., and Risold, P.Y. (2019). The claustrum is a target for projections from the supramammillary nucleus in the rat. Neuroscience *409*, 261–275. https://doi.org/10.1016/j.neuroscience.2019.03.045.

25. Graf, M., Wong, K.L.L., and Augustine, G.J. (2020). Neuroscience: A Role for the Claustrum in Drug Reward. Curr. Biol. *30*, R1038–R1040. https://doi.org/10.1016/j.cub.2020.07.031.

26. McKenna, J.T., and Vertes, R.P. (2004). Afferent projections to nucleus reuniens of the thalamus. J. Comp. Neurol. *480*, 115–142. https://doi.org/10.1002/cne.20342.

27. Narikiyo, K., Mizuguchi, R., Ajima, A., Shiozaki, M., Hamanaka, H., Johansen, J.P., Mori, K., and Yoshihara, Y. (2020). The claustrum coordinates cortical slow-wave activity. Nat. Neurosci. *23*, 741–753. https://doi.org/10.1038/s41593-020-0625-7.

28. Vertes, R.P., and Hoover, W.B. (2008). Projections of the paraventricular and paratenial nuclei of the dorsal midline thalamus in the rat. J. Comp. Neurol. *508*, 212–237. https://doi.org/10.1002/cne.21679.

29. Crick, F.C., and Koch, C. (2005). What is the function of the claustrum? Philos. Trans. R. Soc. Lond. B Biol. Sci. *360*, 1271–1279. https://doi.org/10.1098/rstb.2005.1661.

30. Edelstein, L.R., and Denaro, F.J. (2004). The claustrum: a historical review of its anatomy, physiology, cytochemistry and functional significance. Cell. Mol. Biol. (Noisy-le-grand) *50*, 675–702.

31. Goll, Y., Atlan, G., and Citri, A. (2015). Attention: the claustrum. Trends Neurosci. *38*, 486–495. https://doi.org/10.1016/j.tins.2015.05.006.

32. Jackson, J., Smith, J.B., and Lee, A.K. (2020). The Anatomy and Physiology of Claustrum-Cortex Interactions. Annu. Rev. Neurosci. *43*, 231–247. https://doi.org/10.1146/annurev-neuro-092519-101637.

33. Mathur, B.N. (2014). The claustrum in review. Front. Syst. Neurosci. *8*, 48. https://doi.org/10.3389/fnsys.2014.00048.

34. Patru, M.C., and Reser, D.H. (2015). A New Perspective on Delusional States – Evidence for Claustrum Involvement. Front. Psychiatry *6*, 158. https://doi.org/10.3389/fpsyt.2015.00158.

35. Smith, J.B., Watson, G.D.R., Liang, Z., Liu, Y., Zhang, N., and Alloway, K.D. (2019). A Role for the Claustrum in Salience Processing? Front. Neuroanat. *13*, 64. https://doi.org/10.3389/fnana.2019.00064.

36. Atilgan, H., Doody, M., Oliver, D.K., McGrath, T.M., Shelton, A.M., Echeverria-Altuna, I., Tracey, I., Vyazovskiy, V.V., Manohar, S.G., and Packer, A.M. (2022). Human lesions and animal studies link the claustrum to perception, salience, sleep and pain. Brain *145*, 1610–1623. https://doi.org/10.1093/brain/awac114.

37. Xu, Q.Y., Zhang, H.L., Du, H., Li, Y.C., Ji, F.H., Li, R., and Xu, G.Y. (2022). Identification of a Glutamatergic Claustrum-Anterior Cingulate Cortex Circuit for Visceral Pain Processing. J. Neurosci. *42*, 8154–8168. https://doi.org/10.1523/JNEUROSCI.0779-22.2022.

38. Ntamati, N.R., Acuña, M.A., and Nevian, T. (2023). Pain-induced adaptations in the claustro-cingulate pathway. Cell Rep. *42*, 112506. https://doi.org/10.1016/j.celrep.2023.112506.

39. Fenk, L.A., Riquelme, J.L., and Laurent, G. (2023). Interhemispheric competition during sleep. Nature *616*, 312–318. https://doi.org/10.1038/s41586-023-05827-w.

40. Chevée, M., Finkel, E.A., Kim, S.J., O'Connor, D.H., and Brown, S.P. (2022). Neural activity in the mouse claustrum in a cross-modal sensory

selection task. Neuron *110*, 486–501.e7. https://doi.org/10.1016/j.neuron.2021.11.013.

41. Bickel, S., and Parvizi, J. (2019). Electrical stimulation of the human claustrum. Epilepsy Behav. *97*, 296–303. https://doi.org/10.1016/j.yebeh.2019.03.051.
42. Remedios, R., Logothetis, N.K., and Kayser, C. (2010). Unimodal responses prevail within the multisensory claustrum. J. Neurosci. *30*, 12902–12907. https://doi.org/10.1523/JNEUROSCI.2937-10.2010.
43. Remedios, R., Logothetis, N.K., and Kayser, C. (2014). A role of the claustrum in auditory scene analysis by reflecting sensory change. Front. Syst. Neurosci. *8*, 44. https://doi.org/10.3389/fnsys.2014.00044.
44. Atlan, G., Matosevich, N., Peretz-Rivlin, N., Marsh-Yvgi, I., Zelinger, N., Chen, E., Kleinman, T., Bleistein, N., Sheinbach, E., Groysman, M., et al. (2024). Claustrum neurons projecting to the anterior cingulate restrict engagement during sleep and behavior. Nat. Commun. *15*, 5415. https://doi.org/10.1038/s41467-024-48829-6.
45. Kitanishi, T., and Matsuo, N. (2017). Organization of the Claustrum-to-Entorhinal Cortical Connection in Mice. J. Neurosci. *37*, 269–280. https://doi.org/10.1523/JNEUROSCI.1360-16.2016.
46. Faig, C.A., Kim, G.H.K., Do, A.D., Dworsky-Fried, Z., Jackson, J., and Taylor, A.M.W. (2024). Claustrum projections to the anterior cingulate modulate nociceptive and pain-associated behavior. Curr. Biol. *34*, 1987–1995.e4. https://doi.org/10.1016/j.cub.2024.03.044.
47. Stewart, B.W., Keaser, M.L., Lee, H., Margerison, S.M., Cormie, M.A., Moayedi, M., Lindquist, M.A., Chen, S., Mathur, B.N., and Seminowicz, D.A. (2024). Pathological claustrum activity drives aberrant cognitive network processing in human chronic pain. Curr. Biol. *34*, 1953–1966.e6. https://doi.org/10.1016/j.cub.2024.03.021.
48. Atlan, G., Terem, A., Peretz-Rivlin, N., Sehrawat, K., Gonzales, B.J., Pozner, G., Tasaka, G.I., Goll, Y., Refaeli, R., Zviran, O., et al. (2018). The Claustrum Supports Resilience to Distraction. Curr. Biol. *28*, 2752–2762.e7. https://doi.org/10.1016/j.cub.2018.06.068.
49. White, M.G., Panicker, M., Mu, C., Carter, A.M., Roberts, B.M., Dharmasri, P.A., and Mathur, B.N. (2018). Anterior Cingulate Cortex Input to the Claustrum Is Required for Top-Down Action Control. Cell Rep. *22*, 84–95. https://doi.org/10.1016/j.celrep.2017.12.023.
50. Fodoulian, L., Gschwend, O., Huber, C., Mutel, S., Salazar, R.F., Leone, R., Renfer, J.-R., Ekundayo, K., Rodriguez, I., and Carleton, A. (2020). The claustrum-medial prefrontal cortex network controls attentional set-shifting. Preprint at bioRxiv, 2020.2010.2014.339259. https://doi.org/10.1101/2020.10.14.339259.
51. Zhu, J., Hafycz, J., Keenan, B.T., Guo, X., Pack, A., and Naidoo, N. (2020). Acute Sleep Loss Upregulates the Synaptic Scaffolding Protein, Homer1a, in Non-canonical Sleep/Wake Brain Regions, Claustrum, Piriform and Cingulate Cortices. Front. Neurosci. *14*, 188. https://doi.org/10.3389/fnins.2020.00188.
52. Norimoto, H., Fenk, L.A., Li, H.H., Tosches, M.A., Gallego-Flores, T., Hain, D., Reiter, S., Kobayashi, R., Macias, A., Arends, A., et al. (2020). A claustrum in reptiles and its role in slow-wave sleep. Nature *578*, 413–418. https://doi.org/10.1038/s41586-020-1993-6.
53. Renouard, L., Billwiller, F., Ogawa, K., Clément, O., Camargo, N., Abdelkarim, M., Gay, N., Scoté-Blachon, C., Touré, R., Libourel, P.A., et al. (2015). The supramammillary nucleus and the claustrum activate the cortex during REM sleep. Sci. Adv. *1*, e1400177. https://doi.org/10.1126/sciadv.1400177.
54. Luppi, P.H., Billwiller, F., and Fort, P. (2017). Selective activation of a few limbic structures during paradoxical (REM) sleep by the claustrum and the supramammillary nucleus: evidence and function. Curr. Opin. Neurobiol. *44*, 59–64. https://doi.org/10.1016/j.conb.2017.03.002.
55. Liu, J., Wu, R., Johnson, B., Vu, J., Bass, C., and Li, J.X. (2019). The Claustrum-Prefrontal Cortex Pathway Regulates Impulsive-Like Behavior. J. Neurosci. *39*, 10071–10080. https://doi.org/10.1523/JNEUROSCI.1005-19.2019.
56. Fodoulian, L., Boillat, M., Moulinier, M., Carleton, A., and Rodriguez, I. (2024). A spatial single-cell atlas of the claustro-insular region uncovers key regulators of neuronal identity and excitability. Preprint at bioRxiv. https://doi.org/10.1101/2024.11.05.622016.
57. Jackson, J., Karnani, M.M., Zemelman, B.V., Burdakov, D., and Lee, A.K. (2018). Inhibitory Control of Prefrontal Cortex by the Claustrum. Neuron *99*, 1029–1039.e4. https://doi.org/10.1016/j.neuron.2018.07.031.
58. Cortimiglia, R., Crescimanno, G., Salerno, M.T., and Amato, G. (1991). The role of the claustrum in the bilateral control of frontal oculomotor neurons in the cat. Exp. Brain Res. *84*, 471–477. https://doi.org/10.1007/BF00230958.
59. Ptito, M., and Lassonde, M.C. (1981). Effects of claustral stimulation on the properties of visual cortex neurons in the cat. Exp. Neurol. *73*, 315–320. https://doi.org/10.1016/0014-4886(81)90066-2.
60. Salerno, M.T., Cortimiglia, R., Crescimanno, G., Amato, G., and Infantellina, F. (1984). Effects of claustrum stimulation on spontaneous bioelectrical activity of motor cortex neurons in the cat. Exp. Neurol. *86*, 227–239. https://doi.org/10.1016/0014-4886(84)90183-3.
61. Sherk, H., and LeVay, S. (1983). Contribution of the cortico-claustral loop to receptive field properties in area 17 of the cat. J. Neurosci. *3*, 2121–2127. https://doi.org/10.1523/JNEUROSCI.03-11-02121.1983.
62. Tsumoto, T., and Suda, K. (1982). Effects of stimulation of the dorsocaudal claustrum on activities of striate cortex neurons in the cat. Brain Res. *240*, 345–349. https://doi.org/10.1016/0006-8993(82)90233-5.
63. Graf, M., Nair, A., Wong, K.L.L., Tang, Y., and Augustine, G.J. (2020). Identification of Mouse Claustral Neuron Types Based on Their Intrinsic Electrical Properties20. eNeuro *7*, 216. https://doi.org/10.1523/ENEURO.0216-20.2020.
64. Erwin, S.R., Bristow, B.N., Sullivan, K.E., Kendrick, R.M., Marriott, B., Wang, L., Clements, J., Lemire, A.L., Jackson, J., and Cembrowski, M. S. (2021). Spatially patterned excitatory neuron subtypes and projections of the claustrum. eLife *10*, e68967. https://doi.org/10.7554/eLife.68967.
65. Markram, H., Toledo-Rodriguez, M., Wang, Y., Gupta, A., Silberberg, G., and Wu, C. (2004). Interneurons of the neocortical inhibitory system. Nat. Rev. Neurosci. *5*, 793–807. https://doi.org/10.1038/nrn1519.
66. Ascoli, G.A., Alonso-Nanclares, L., Anderson, S.A., Barrionuevo, G., Benavides-Piccione, R., Burkhalter, A., Buzsáki, G., Cauli, B., Defelipe, J., et al.; Petilla Interneuron Nomenclature Group (2008). Petilla terminology: nomenclature of features of GABAergic interneurons of the cerebral cortex. Nat. Rev. Neurosci. *9*, 557–568. https://doi.org/10.1038/nrn2402.
67. Rudy, B., Fishell, G., Lee, S., and Hjerling-Leffler, J. (2011). Three groups of interneurons account for nearly 100% of neocortical GABAergic neurons. Dev. Neurobiol. *71*, 45–61. https://doi.org/10.1002/dneu.20853.
68. Haider, B., and McCormick, D.A. (2009). Rapid neocortical dynamics: cellular and network mechanisms. Neuron *62*, 171–189. https://doi.org/10.1016/j.neuron.2009.04.008.
69. Hasenstaub, A., Shu, Y., Haider, B., Kraushaar, U., Duque, A., and McCormick, D.A. (2005). Inhibitory postsynaptic potentials carry synchronized frequency information in active cortical networks. Neuron *47*, 423–435. https://doi.org/10.1016/j.neuron.2005.06.016.
70. Lee, S., Hjerling-Leffler, J., Zagha, E., Fishell, G., and Rudy, B. (2010). The largest group of superficial neocortical GABAergic interneurons expresses ionotropic serotonin receptors. J. Neurosci. *30*, 16796–16808. https://doi.org/10.1523/JNEUROSCI.1869-10.2010.
71. Pouille, F., and Scanziani, M. (2001). Enforcement of temporal fidelity in pyramidal cells by somatic feed-forward inhibition. Science *293*, 1159–1163. https://doi.org/10.1126/science.1060342.
72. Urban-Ciecko, J., and Barth, A.L. (2016). Somatostatin-expressing neurons in cortical networks. Nat. Rev. Neurosci. *17*, 401–409. https://doi.org/10.1038/nrn.2016.53.
73. Wang, Y.J., Zan, G.Y., Xu, C., Li, X.P., Shu, X., Yao, S.Y., Xu, X.S., Qiu, X., Chen, Y., Jin, K., et al. (2023). The claustrum-prelimbic cortex circuit through dynorphin/kappa-opioid receptor signaling underlies

depression-like behaviors associated with social stress etiology. Nat. Commun. *14*, 7903. https://doi.org/10.1038/s41467-023-43636-x.

74. Xu, J., Jo, A., DeVries, R.P., Deniz, S., Cherian, S., Sunmola, I., Song, X., Marshall, J.J., Gruner, K.A., Daigle, T.L., et al. (2022). Intersectional mapping of multi-transmitter neurons and other cell types in the brain. Cell Rep. *40*, 111036. https://doi.org/10.1016/j.celrep.2022.111036.
75. Lemon, R.N., Baker, S.N., and Kraskov, A. (2021). Classification of Cortical Neurons by Spike Shape and the Identification of Pyramidal Neurons. Cereb. Cortex *31*, 5131–5138. https://doi.org/10.1093/cercor/bhab147.
76. Petreanu, L., Mao, T., Sternson, S.M., and Svoboda, K. (2009). The subcellular organization of neocortical excitatory connections. Nature *457*, 1142–1145. https://doi.org/10.1038/nature07709.
77. Oh, S.W., Harris, J.A., Ng, L., Winslow, B., Cain, N., Mihalas, S., Wang, Q., Lau, C., Kuan, L., Henry, A.M., et al. (2014). A mesoscale connectome of the mouse brain. Nature *508*, 207–214. https://doi.org/10.1038/nature13186.
78. Tremblay, R., Lee, S., and Rudy, B. (2016). GABAergic Interneurons in the Neocortex: From Cellular Properties to Circuits. Neuron *91*, 260–292. https://doi.org/10.1016/j.neuron.2016.06.033.
79. Riedemann, T., Schmitz, C., and Sutor, B. (2016). Immunocytochemical heterogeneity of somatostatin-expressing GABAergic interneurons in layers II and III of the mouse cingulate cortex: A combined immunofluorescence/design-based stereologic study. J. Comp. Neurol. *524*, 2281–2299. https://doi.org/10.1002/cne.23948.
80. Wu, S.J., Sevier, E., Dwivedi, D., Saldi, G.A., Hairston, A., Yu, S., Abbott, L., Choi, D.H., Sherer, M., Qiu, Y., et al. (2023). Cortical somatostatin interneuron subtypes form cell-type-specific circuits. Neuron *111*, 2675–2692.e9. https://doi.org/10.1016/j.neuron.2023.05.032.
81. Hur, E.E., and Zaborszky, L. (2005). Vglut2 afferents to the medial prefrontal and primary somatosensory cortices: a combined retrograde tracing in situ hybridization study [corrected]. J. Comp. Neurol. *483*, 351–373. https://doi.org/10.1002/cne.20444.
82. Le Merre, P., Esmaeili, V., Charrière, E., Galan, K., Salin, P.A., Petersen, C.C.H., and Crochet, S. (2018). Reward-Based Learning Drives Rapid Sensory Signals in Medial Prefrontal Cortex and Dorsal Hippocampus Necessary for Goal-Directed Behavior. Neuron *97*, 83–91.e5. https://doi.org/10.1016/j.neuron.2017.11.031.
83. Einevoll, G.T., Kayser, C., Logothetis, N.K., and Panzeri, S. (2013). Modelling and analysis of local field potentials for studying the function of cortical circuits. Nat. Rev. Neurosci. *14*, 770–785. https://doi.org/10.1038/nrn3599.
84. Buzsáki, G., Anastassiou, C.A., and Koch, C. (2012). The origin of extracellular fields and currents–EEG, ECoG, LFP and spikes. Nat. Rev. Neurosci. *13*, 407–420. https://doi.org/10.1038/nrn3241.
85. Pfeffer, C.K., Xue, M., He, M., Huang, Z.J., and Scanziani, M. (2013). Inhibition of inhibition in visual cortex: the logic of connections between molecularly distinct interneurons. Nat. Neurosci. *16*, 1068–1076. https://doi.org/10.1038/nn.3446.
86. Kvitsiani, D., Ranade, S., Hangya, B., Taniguchi, H., Huang, J.Z., and Kepecs, A. (2013). Distinct behavioural and network correlates of two interneuron types in prefrontal cortex. Nature *498*, 363–366. https://doi.org/10.1038/nature12176.
87. Pi, H.J., Hangya, B., Kvitsiani, D., Sanders, J.I., Huang, Z.J., and Kepecs, A. (2013). Cortical interneurons that specialize in disinhibitory control. Nature *503*, 521–524. https://doi.org/10.1038/nature12676.
88. Cauller, L.J., and Kulics, A.T. (1991). The neural basis of the behaviorally relevant N1 component of the somatosensory-evoked potential in SI cortex of awake monkeys: evidence that backward cortical projections signal conscious touch sensation. Exp. Brain Res. *84*, 607–619. https://doi.org/10.1007/BF00230973.
89. Gilbert, C.D., and Sigman, M. (2007). Brain states: top-down influences in sensory processing. Neuron *54*, 677–696. https://doi.org/10.1016/j.neuron.2007.05.019.
90. Jiang, X., Wang, G., Lee, A.J., Stornetta, R.L., and Zhu, J.J. (2013). The organization of two new cortical interneuronal circuits. Nat. Neurosci. *16*, 210–218. https://doi.org/10.1038/nn.3305.
91. Larkum, M.E. (2013). The yin and yang of cortical layer 1. Nat. Neurosci. *16*, 114–115. https://doi.org/10.1038/nn.3317.
92. Lee, A.J., Wang, G., Jiang, X., Johnson, S.M., Hoang, E.T., Lanté, F., Stornetta, R.L., Beenhakker, M.P., Shen, Y., and Julius Zhu, J. (2015). Canonical Organization of Layer 1 Neuron-Led Cortical Inhibitory and Disinhibitory Interneuronal Circuits. Cereb. Cortex *25*, 2114–2126. https://doi.org/10.1093/cercor/bhu020.
93. Letzkus, J.J., Wolff, S.B.E., Meyer, E.M.M., Tovote, P., Courtin, J., Herry, C., and Lüthi, A. (2011). A disinhibitory microcircuit for associative fear learning in the auditory cortex. Nature *480*, 331–335. https://doi.org/10.1038/nature10674.
94. Garcia-Munoz, M., and Arbuthnott, G.W. (2015). Basal ganglia-thalamus and the "crowning enigma". Front. Neural Circuits *9*, 71. https://doi.org/10.3389/fncir.2015.00071.
95. Shepherd, G.M.G. (2013). Corticostriatal connectivity and its role in disease. Nat. Rev. Neurosci. *14*, 278–291. https://doi.org/10.1038/nrn3469.
96. Mantas, I., Flais, I., Masarapu, Y., Ionescu, T., Frapard, S., Jung, F., Le Merre, P., Saarinen, M., Tiklova, K., Salmani, B.Y., et al. (2024). Claustrum and dorsal endopiriform cortex complex cell-identity is determined by Nurr1 and regulates hallucinogenic-like states in mice. Nat. Commun. *15*, 8176. https://doi.org/10.1038/s41467-024-52429-9.
97. White, M.G., Mu, C., Qadir, H., Madden, M.B., Zeng, H., and Mathur, B.N. (2020). The Mouse Claustrum Is Required for Optimal Behavioral Performance Under High Cognitive Demand. Biol. Psychiatry *88*, 719–726. https://doi.org/10.1016/j.biopsych.2020.03.020.
98. Shipp, S. (2007). Structure and function of the cerebral cortex. Curr. Biol. *17*, R443–R449. https://doi.org/10.1016/j.cub.2007.03.044.
99. Beul, S.F., and Hilgetag, C.C. (2014). Towards a "canonical" agranular cortical microcircuit. Front. Neuroanat. *8*, 165. https://doi.org/10.3389/fnana.2014.00165.
100. Pachitariu, M., Steinmetz, N., Kadir, S., Carandini, M., Kenneth, D., and H. (2016). Kilosort: realtime spike-sorting for extracellular electrophysiology with hundreds of channels. Preprint at bioRxiv, 061481. https://doi.org/10.1101/061481.
101. Rossant, C., Kadir, S.N., Goodman, D.F.M., Schulman, J., Hunter, M.L. D., Saleem, A.B., Grosmark, A., Belluscio, M., Denfield, G.H., Ecker, A. S., et al. (2016). Spike sorting for large, dense electrode arrays. Nat. Neurosci. *19*, 634–641. https://doi.org/10.1038/nn.4268.
102. Hippenmeyer, S., Vrieseling, E., Sigrist, M., Portmann, T., Laengle, C., Ladle, D.R., and Arber, S. (2005). A developmental switch in the response of DRG neurons to ETS transcription factor signaling. PLOS Biol. *3*, e159. https://doi.org/10.1371/journal.pbio.0030159.
103. Taniguchi, H., He, M., Wu, P., Kim, S., Paik, R., Sugino, K., Kvitsiani, D., Fu, Y., Lu, J., Lin, Y., et al. (2011). A resource of Cre driver lines for genetic targeting of GABAergic neurons in cerebral cortex. Neuron *71*, 995–1013. https://doi.org/10.1016/j.neuron.2011.07.026.
104. Gerfen, C.R., Paletzki, R., and Heintz, N. (2013). GENSAT BAC cre-recombinase driver lines to study the functional organization of cerebral cortical and basal ganglia circuits. Neuron *80*, 1368–1383. https://doi.org/10.1016/j.neuron.2013.10.016.
105. Milstein, A.D., Bloss, E.B., Apostolides, P.F., Vaidya, S.P., Dilly, G.A., Zemelman, B.V., and Magee, J.C. (2015). Inhibitory Gating of Input Comparison in the CA1 Microcircuit. Neuron *87*, 1274–1289. https://doi.org/10.1016/j.neuron.2015.08.025.
106. Madisen, L., Zwingman, T.A., Sunkin, S.M., Oh, S.W., Zariwala, H.A., Gu, H., Ng, L.L., Palmiter, R.D., Hawrylycz, M.J., Jones, A.R., et al. (2010). A robust and high-throughput Cre reporting and characterization system for the whole mouse brain. Nat. Neurosci. *13*, 133–140. https://doi.org/10.1038/nn.2467.

107. Vong, L., Ye, C., Yang, Z., Choi, B., Chua, S., Jr., and Lowell, B.B. (2011). Leptin action on GABAergic neurons prevents obesity and reduces inhibitory tone to POMC neurons. Neuron *71*, 142–154. https://doi.org/10.1016/j.neuron.2011.05.028.

108. Jun, J.J., Steinmetz, N.A., Siegle, J.H., Denman, D.J., Bauza, M., Barbarits, B., Lee, A.K., Anastassiou, C.A., Andrei, A., Aydın, Ç., et al. (2017). Fully integrated silicon probes for high-density recording of neural activity. Nature *551*, 232–236. https://doi.org/10.1038/nature24636.

109. Vinck, M., Batista-Brito, R., Knoblich, U., and Cardin, J.A. (2015). Arousal and locomotion make distinct contributions to cortical activity patterns and visual encoding. Neuron *86*, 740–754. https://doi.org/10.1016/j.neuron.2015.03.028.

110. Wang, Q., Ding, S.L., Li, Y., Royall, J., Feng, D., Lesnar, P., Graddis, N., Naeemi, M., Facer, B., Ho, A., et al. (2020). The Allen Mouse Brain Common Coordinate Framework: A 3D Reference Atlas. Cell *181*, 936–953.e20. https://doi.org/10.1016/j.cell.2020.04.007.

111. Puchades, M.A., Csucs, G., Ledergerber, D., Leergaard, T.B., and Bjaalie, J.G. (2019). Spatial registration of serial microscopic brain images to three-dimensional reference atlases with the QuickNII tool. PLOS One *14*, e0216796. https://doi.org/10.1371/journal.pone.0216796.

STAR★METHODS

KEY RESOURCES TABLE

REAGENT or RESOURCE	SOURCE	IDENTIFIER
Antibodies		
Biocytin (ε-Biotinoyl-L-Lysine)	ThermoFisher	Cat. # B1592
Cy5-conjugated streptavidin	Jackson ImmunoResearch Laboratories	RRID: AB_2337245
DAPI (4′,6-diamidino-2-fenilindol, dihidrocloruro)	ThermoFisher	Cat. # D1306; RRID AB_2629482
Bacterial and virus strains		
pAAV2-CaMKIIa-hChR2(H134R)-EYFP	Karl Deisseroth	Cat. # 26969-AAV2; RRID:Addgene_26969
AAV5.EF1.dflox.hChR2(H134R)-mCherry.WPRE.hGH	Karl Deisseroth	Cat. # 20297; RRID: Addgene_20297
AAV5.EF1.dflox.hChR2(H134R)-eYFP.WPRE.hGH	Karl Deisseroth	Cat. # 20298; RRID: Addgene_20298
pAAV-hSyn-DIO-mCherry	Addgene	Cat. # 50459; RRID:Addgene_50459
Red Retrobeads	Lumafluor	https://lumafluor.com/
Chemicals, peptides, and recombinant proteins		
Isoflurane, Forene	AbbVie AB (Solna, Sweden)	Cat. #: 506949
Sodium pentobarbital	APL AB (Stockholm, Sweden)	Cat. #: 338327
Temgesic 0.3mg/ml	Indivior Europe Limited (Apoteket)	Cat. # 521634
Viscotears 2mg/g	Thea (Apoteket)	Cat. #: 569173
Xylocain Spray 100 mg/ml	AstraZeneca	Cat. #: 469429
Adhese Universal Refill Bottle 2x5g	IvoClar Vivadent	Cat. #: 663721WW
Dental cement, Tetric EvoFlow, 1x 2 g	IvoClar Vivadent	Cat. #: 595953WW
Silicone sealant Kwik-Cast	WPI	Cat. #: KWIK-CAST
D-APV	Tocris	Cat. # 79055-68-8
NBQX disodium salt	Tocris	Cat. # 479347-86-9
Tetrodotoxin citrate (TTX)	Tocris	Cat. # 18660-81-6
4-Aminopyridine (4AP)	Tocris	Cat. # 504-24-5
SR-95531 (Gabazine)	Merck	Cat. # 104104-50-9
DiI (1,1′-dioctadecyl-3,3,3′3’-tetramethylindocarbocyanine perchlorate)	Invitrogen, ThermoFisher	Cat. # D282
Critical commercial assays		
RNAscope Multiplex Fluorescent v2	ACD	Cat. # 323100
Probe- Mm-Slc17a6-C1	ACD	Cat. # 319171
Probe- Mm-CamkIIa-C2	ACD	Cat. # 445231
TSA Cyanine 3	Akoya Biosciences	Cat. #NEL744001KT
TSA Cyanine 5	Akoya Biosciences	Cat. #NEL745001KT
Experimental models: Organisms/strains		
Mouse, C57BL/6J	The Jackson Laboratory	RRID: IMSR_JAX: 000664
Mouse, PV-Cre	The Jackson Laboratory	RRID: IMSR_JAX:017320
Mouse, SOM-Cre	The Jackson Laboratory	RRID: IMSR_JAX:018973
Mouse, Ai9 (RCL-tdT)	The Jackson Laboratory	RRID: IMSR_JAX:007909
Mouse, NPY-Cre	The Jackson Laboratory	RRID: IMSR_JAX:027851
Mouse, 5Ht3a-Cre	The Rockefeller University, GENSAT	RRID: MMRRC_036680-UCD
Mouse, Vglut2-ires-cre	The Jackson Laboratory	RRID: IMSR_JAX:016963
Software and algorithms		
ImageJ FIJI	NIH	https://imagej.nih.gov/ij
QuickNII	NITRC	https://quicknii.readthedocs.io/
VisuAlign	NITRC	https://visualign.readthedocs.io
Python	Python Software Foundation	https://www.python.org/

(*Continued on next page*)

Continued

REAGENT or RESOURCE	SOURCE	IDENTIFIER
Anaconda	Anaconda Inc.	https://www.anaconda.com/
Open Ephys GUI	Open Ephys	https://open-ephys.org/gui
Kilosort2.5	Pachitariu. et al.[100]	https://github.com/MouseLand/Kilosort
Matlab 2020a	Mathworks	https://mathworks.com
Graphpad Prism 8.0.1	Graphpad Software	https://www.graphpad.com
ZEN Blue 2.3	Carl Zeiss	https://www.zeiss.com/
CorelDraw X8	Corel Corporation	https://www.coreldraw.com
Igor Pro 6.37	Wavemetrics	https://www.wavemetrics.com/
Phy2	Rossant et al.[101]	https://github.com/cortex-lab/phy

EXPERIMENTAL MODEL AND STUDY PARTICIPANT DETAILS

All experiments were performed according to the Guidelines of the Stockholm municipal committee for animal experiments. 40 adult PV-Cre (B6.129P2-Pvalbtm1(cre)Arbr/J, The Jackson Laboratory, IMSR_JAX:017320),[102] 11 adult SOM-Cre mice (B6N.Cg-Ssttm2.1 (cre)Zjh/J, The Jackson Laboratory, IMSR_JAX:018973),[103] 30 adult 5HT3a-Cre (Tg(Htr3a-cre)NO152Gsat/Mmucd, GENSAT, MMRRC_036680-UCD)[104] mice and 15 adult NPY-Cre (B6.Cg-Npytm1(cre)Zman/J, The Jackson Laboratory, IMSR_JAX:027851)[105] were crossed with tdTomato reporter mouse line (B6.Cg-Gt(ROSA)26Sortm9(CAG-tdTomato)Hze/J, The Jackson Laboratory, MSR_JAX:007909)[106] to obtain transgenic interneuron reporter mice. 29 adult VGLUT2-Cre (Slc17a6tm2(cre)Lowl/J, The Jackson Laboratory, IMSR_JAX:016963)[107] transgenic mice of both sexes were used to study the effect of VGLUT2-expressing CLA projection neurons on the ACC.

METHOD DETAILS

Virus injection

Mice of either sex, 6-8 weeks old, were anesthetized with isoflurane and placed in a stereotaxic frame (Harvard Apparatus). To target the CLA, a craniotomy was made -0.7 mm anterior-posterior (A/P) to bregma, + 3.4 mm medio-lateral (M/L) to the midline and 4.2 mm dorso-ventral (D/V) from the skull. A total of 100 nl of virus AAV2-CaMKIIa-hChR2(H134R)-EYFP (Addgene:26969-AAV2) for PV, SOM, 5HT3a, and NPY Cre- transgenic mice and AAV5.EF1.dflox.hChR2(H134R)-eYFP.WPRE.hGH (Addgene:20298) for VGLUT2-Cre mice was injected by a micropipette using Quintessential Stereotaxic Injector (Stoelting Europe) at a rate of 300 nl/min. To target the ACC a craniotomy was made 0.7 mm anterior to bregma, 0.25 mm lateral to midline and 1.4 mm ventral. Two types of injections were made in the ACC. To identify ACC-projecting CLA neurons in the VGLUT2-Cre mice, red retrograde beads (Lumafluor) were injected into the ACC at the above-mentioned craniotomy. The pipette was held in place for 3 mins after the injection before being slowly retracted from the brain. Post injection analgesics were given (0.03 mg/kg buprenorphine, Eumedica).

Head implants

Adult mice (2 to 3 months old) were anesthetized with isofluorane (AbbVie AB), and the head was fixed in a stereotaxic apparatus (Stoelting). Temgesic (0.03 mg/kg, Eumedica) was administered before the surgery. The body temperature was maintained at 36 and 37°C by a heating pad. To avoid ocular dehydration, an ocular ointment (Viscotears 2 mg/g, Thea) was applied over the eyes. To reduce any possible pain sensation, lidocaine was applied on the skin surface before the incision (AstraZeneca). After removing the skin covering the regions of interest, the bone was gently cleaned. Targeted regions for optic fiber placement and electrophysiological recordings were marked using stereotaxic coordinates on the surface of the skull. ACC craniotomy coordinates for recordings: ACC layer 2/3: +0.5 mm A/P and +0.2 mm M/L; ACC layer 5/6: +0.5 mm A/P and +0.5 mm M/L. Optic fiber craniotomy coordinates: +0.5 mm A/P and +0.2 mm M/L. Then, a thin layer of light-curing adhesive (Ivoclar Vivadent) was applied on the exposed skull. An aluminum metal head-post was fixed with dental cement Tetric Evo (Ivoclar Vivadent) between hemispheres close to mid-sagittal suture. A wall of dental cement was built along the edge of the bone and covering the implant. After the surgery, the animals were returned to their home cage.

In vivo electrophysiology

Following a recovery period of at least three days after implantation, mice were habituated to being head-restrained over a period of 3-4 days. The recordings were performed up to 7 days after the habituation. On the day of the experiments, mice were anesthetized with isoflurane (AbbVie AB) and small craniotomies (300-500 μm in diameter) were drilled to access the targeted areas. The open craniotomies were covered with silicone sealant (Kwik-Cast, WPI), and the animals were returned to their home cages for recovery. After 2 to 4 hours of recovery, mice were head-fixed, and the silicone from the craniotomies was removed. Extracellular LFP and spikes in the ACC were recorded using a silicon probe (A1x32-Poly2-5mm-50 s-177 and A1xOA32LP-Poly2-5mm-50 s-177,

NeuroNexus) with 32 electrodes inserted 1.3 mm deep from the surface at the ACC L2/3 coordinates (+0.5 mm A-P; 0.25 mm M-L) or 1.5 mm deep from the surface at the ACC L5/6 coordinates (+0.5 mm A-P; 0.45 mm M-L). The probe was lowered using a micromanipulator (Luigs and Neumann) at a low speed (1 μm/s), to minimize damage to the brain tissue. To allow the brain to recover from the mechanical strain of the probe insertion, the recordings started 30 minutes after the probe was in its required position. The craniotomies were always covered with saline to avoid the dryness of the surface. The electrode reference was then connected to a silver wire positioned over the pia in a second craniotomy near the cerebellum with a second micromanipulator. The probe and the optic fiber were coated with DiI (1,1'-dioctadecyl-3,3,3′3'-tetramethylindocarbocyanine perchlorate, Invitrogen) for post hoc recovery of the recording location. The signals were filtered between 0.3 Hz and 7.5 kHz and amplified using a digital head stage (RDH2132, Intan Technologies) and OpenEphys software. Broadband activity was sampled at 30 kHz (band pass filtered between 0.3 Hz and 7.5 kHz by the amplifier) and stored for offline analysis. A maximum of two recordings, one in layer 2/3 and another in layer 5/6, were performed in the same animal and same day before they were sacrificed. Probes were cleaned with 1% Tergazyme (Sigma-Aldrich) for at least 24 hours following the recording, then rinsed with deionized water.

In vivo photostimulation

In the *in vivo* experiments, CLA cell bodies were stimulated 150 times with 5 ms duration light pulses delivered in a 5-second inter-trial interval through an optical fiber (NA 0.5, 200 μm diameter) located above the CLA. The optical fiber was connected to a light-emitting diode (LED, 470 nm, Prizmatix) through a patch cable (NA 0.5., core diameters: 250 μm, Prizmatix). The LED was controlled by the Spike2 program (Cambridge Electronic Design). Simultaneously, the ACC activity was recorded as described above (Methods; *in vivo* electrophysiology). At the end of the protocol, the recording was stopped. If no changes in the LFP activity were detected online, the probe was moved 100-200 μm deeper and then repeated the stimulation protocol. To corroborate that CLA was activated, in some experiments, 5 ms and 500 ms duration light pulses were delivered every 5 seconds at least 40 times directly into the CLA using a silicon probe attached to an optical fiber (A1xOA32LP-Poly2-5mm-50 s-177, NeuroNexus). If no optotagged units were observed online, the probe was lowered at a low speed (1 μm/sec) for a maximum of 200 μm and repeated the photostimulation. Our criteria for determining whether CLA was activated was a positive change in firing rate in the units in the 1-10 ms window after 5 ms photostimulation. In the 500 ms protocol, some units sustained the activity while photostimulation was evoked. Others adapted a few milliseconds after the initiation. At the end of the experiment, the virus expression was corroborated. If no CLA fibers were observed in the ACC, or if the injection was predominantly out of the CLA, the animal was removed from the study.

Spike sorting

Recordings acquired in OpenEphys were processed using the standard Kilosort 2.5 pipeline for spike detection, drift tracking, and clustering.[100] Following automated sorting, all units were manually curated using Phy2.[101,108] Units were considered putative single units if they exhibited clear physiological and statistical signatures of well-isolated neurons.

We included only those units with fewer than 1% of inter-spike intervals (ISIs) shorter than 2 ms, indicating minimal refractory period violations. In addition, the waveform had to be clearly distinguishable from background noise, with a peak-to-peak amplitude greater than 125 μV. We verified the consistency of spike waveforms over time and across events, excluding clusters with mixed or unstable shapes. Cluster quality was further assessed using principal component projections; only units with well-isolated clusters and minimal overlap with neighboring units were retained. Units that did not meet these criteria were classified as multi-unit activity (MUA) or noise and excluded from further analysis. Optogenetic activation of VGLUT2 and CaMKIIa were aligned with electrophysiological recordings using event times recorded using OpenEphys. Probe trajectory was estimated from histology and Allen Brain Atlas.[77] Single unit activity which occurred within layer 2/3 or layer 5 were selected for further analysis. The waveforms for each single unit activity were combined individually and an average waveform was calculated. The spike width was calculated as the duration between the maximum amplitude and the repolarization to baseline. A histogram was plotted which showed a bimodal distribution of spike widths, the spike width of 0.6 ms was chosen as the threshold and used for the separation of FS and RS.[57] Single-unit firing frequency was calculated using 10 ms bins and a Gaussian kernel (sigma=10 ms), then converted to z-scores. Neuronal responses to CLA activation were categorized as excitation, inhibition, or no modulation based on z-score changes within 30 ms post-stimulation. Excitation was defined as any 10 ms bin within the first 30 ms post-stimulation with a firing rate exceeding a z-score value of 4 (4 standard deviations). Neurons were classified as inhibited if, within the 30 ms period following CLA activation, any 10 ms bin exhibited a firing rate lower than two standard deviations below the mean baseline firing rate (-2 z-score). Neurons previously identified as exhibiting excitation were excluded from this inhibition analysis. Neurons not meeting criteria for either excitation or inhibition were categorized as showing no modulation.

Modulation index calculations

The CLA modulation index (MI) was calculated using the formula (FRpost – FRbase) / (FRpost + FR FRbase).[57,109] This index ranges from −1, indicating total suppression, to values near 1, reflecting robust neuronal excitation. Baseline firing activity (FRbase) was calculated as the average firing rate during the one second immediately preceding CLA stimulation, while post-stimulation activity (FRpost) was determined from the mean firing rate in the first 100 milliseconds following activation. A separate modulation index was also computed based on a 30-millisecond time window, which was specifically chosen to assess the direct activation of ACC neurons following CLA stimulation.

Brain slice preparation

Mice were incubated for at least 21 days post-surgery following which the mice were sacrificed and used for *ex vivo* recordings. Mice were anesthetized with isoflurane and their brains removed in ice-cold cutting solution containing the following (in mM): 2.5 KCl, 1.25 NaH_2PO_4, 0.5 $CaCl_2$, 7.5 $MgCl_2$, 10 glucose, 25 $NaHCO_3$, 205 sucrose. Coronal slices, 250 μm thick, were cut (Leica VT 1000S, Wetzlar), then transferred to a 35°C water bath for 1 h in artificial CSF containing the following (in mM): 125 NaCl, 25 glucose, 25 $NaHCO_3$, 2.5 KCl, 2 $CaCl_2$, 1.25 NaH_2PO_4, 1 $MgCl_2$. Slices were initially maintained at room temperature for a minimum of 30 minutes. Subsequently, they were transferred to a bath of artificial CSF containing 10 μM gabazine for experiments and used within 12 hours after the brain was sliced. Reagents were obtained from Sigma-Aldrich.

Whole-cell patch-clamp recordings

Whole-cell patch-clamp recordings were obtained at 35 ± 0.5°C. Glass electrodes were pulled with a Flaming/Brown micropipette puller P-97 (Sutter Instruments) and had a resistance of 7–9MΩ. They contained (in mM) 130 K-gluconate, 5 KCl, 10 HEPES, 4 Mg-ATP, 0.3 Na-GTP, 10 Na2-phosphocreatine and 0.3% Neurobiotin. Neurons were visualized with infrared differential interference contrast (IR-DIC) microscopy (Zeiss FS Axioskop) and fluorescent microscopy, using a mercury lamp (HBO 100, Zeiss) and a fluorescent filter cube mounted on the same microscope. Pairs of neurons were recorded within a range of 200 μm from each somata. Recordings were amplified using MultiClamp 700B (Molecular Devices) and digitized by an ITC-18 (HEKA Elektronik) acquisition board. Data was acquired and analyzed using IGOR Pro (WaveMetrics).

Determination of cortical layer

Cortical layers were assigned to every neuron prior to recordings. Layer 1 is defined as the layer closest to the pia with few neurons. Layer 2/3 is defined as a dense layer of neurons next to layer 1. To avoid attribution errors, both infragranular layers 5 and 6 are considered together. Layer 5/6 is defined as neurons located above the cingulum bundle (Figures 3A and S3).

Photostimulation in brain slices

Photostimulation was generated through a 1-watt blue LED (wavelength 465 nm) mounted on the microscope oculars and delivered through the objective lens. Photostimulation was controlled by a LED driver (Mightex Systems) connected to the ITC-18 acquisition board, enabling control over the duration and intensity. The photostimulation diameter through the objective lens was ∼400 μm with an illumination intensity of 16 mW/mm^2 for experiments on VGLUT2 mice and 0.8 mW/mm^2 for all other experiments. Short light pulses (2 ms duration, 8 pulses at 10 Hz, followed by a single 2 ms light flash after another 500 ms) were delivered to evoke post-synaptic responses in neurons; these responses were recorded with the patch pipette. Every experiment was repeated 20 times with 10 second intervals. A recording was determined to receive synaptic input if it showed repeatable stimulus-locked post-synaptic response to photostimulation.

RNAscope *in situ* hybridization

Mice (n=4) were sacrificed with an overdose of sodium pentobarbital (200 mg/kg I.P.) and subsequently perfused transcardially with 4% PFA in 0.01 M PBS. The brains were extracted and kept for an additional 2 h treatment in PFA. The tissue was then washed in PBS and placed in a 25% (w/v) sucrose solution in PBS overnight at 4°C for cryoprotection. Serial 12 μm coronal sections were cut on a cryostat. Sections were mounted on Superfrost Plus microscope slides (Thermo Scientific). In situ hybridization targeting CaMKIIa and VGLUT2 mRNA was conducted using the RNAscope Multiplex Fluorescent v2 Assay Kit (Advanced Cell Diagnostics, Bio-Techne; Cat. #323110), in accordance with the manufacturer's guidelines for fixed-frozen samples. The VGLUT2 transcript (gene symbol: Slc17a6) was labeled using the channel 1 probe (Cat. #319171), with signal amplification achieved via tyramide signal amplification (TSA) conjugated to Cy5 fluorophore. To simultaneously detect CaMKIIa mRNA, a channel 2-specific probe (Cat. #445231-C2) was applied, and visualization was performed using TSA coupled with a Cy3 fluorophore. Following the hybridization procedure, tissue sections were counterstained with DAPI at a dilution of 1:5000 to visualize cell nuclei.

To delineate the anatomical boundaries of the CLA, the Allen Mouse Brain Atlas (Common Coordinate Framework v3, CCFv3) was used as a reference[110]. Acquired images were aligned to the atlas using QuickNII and VisuAlign to ensure accurate spatial correspondence with atlas-defined claustral regions.[111] Quantitative analysis was performed using FIJI (ImageJ). DAPI-stained nuclei were segmented and used as the basis for identifying individual cells. Puncta corresponding to RNA transcripts were assigned to cells if they were either directly overlapping the nucleus or located within approximately 3 μm radius from the nuclear edge. A minimum of three puncta was required for a cell to be classified as positive for a given transcript. In the case of CaMKIIa, low-level background signal was occasionally observed but was excluded from analysis. Only puncta clearly localized around the nucleus were considered. When CaMKIIa puncta were found in dense aggregates that prevented accurate counting, a conservative upper limit of 25 puncta per cell was applied. This threshold exceeded the maximum values observed for VGLUT2-positive cells and was used to standardize comparisons. Quantification was performed on at least 2 coronal sections per animal, sampled across the rostrocaudal extent of the claustrum (n = 4 mice, totaling 1,344 quantified cells). To characterize the distribution of puncta expression intensity, neurons were categorized into four distinct groups based on puncta counts: <3 puncta, indicating minimal or no expression; 3-9 puncta; indicating low expression; 10-15 puncta, indicating medium expression; and >15 puncta, indicating high expression. Pie charts were generated to visualize the relative proportions of neurons within each expression category. The percentages represented in these charts were calculated based on the total number of neurons analyzed (DAPI+), including both puncta-positive and puncta-negative

cells. Venn diagrams were generated (Figure S2) to visualize the overlap of probe expression within CLA cells. Diagram's outer circle represents the total number of cells quantified via DAPI staining, while the inner circles indicate the percentage of these cells positive for each specific probe.

Confocal imaging

Some slices used for *ex vivo* whole-cell patch-clamp recordings were fixed in Lana's fixative (4% PFC with picric acid) in preparation for imaging. Slices were fixed overnight and subsequently washed in PBS 6 times, for 10 minutes each wash. A subset of slices with neurons intracellularly filled with neurobiotin were next incubated in Cy5-PBS (Jackson ImmunoResearch Laboratories) for at least 72 hours. Slices were then mounted on a glass slide with 70% glycerol and DABCO mounting medium. Confocal images were acquired using confocal microscopy (Zeiss LSM 510) and visualized using ImageJ (Fiji).

QUANTIFICATION AND STATISTICAL ANALYSIS

All data are represented as mean ± SEM. All data distribution was first checked for normality (Shapiro-Wilk test) and analyzed accordingly. 2-way ANOVA d and paired two-sample Student's t-test for two-group comparisons. Non-normally distributed data were analyzed by the Mann-Whitney for two-group comparison, Wilcoxon signed-rank test was used for paired samples. Percentages were analyzed using Fisher's exact test. Statistical analyses were done in Prism 8 (GraphPad Software) and Matlab R2020a (Mathworks). Final figures have been assembled with Corel DrawX8 (Corel Corporation) and Adobe Illustrator (Adobe).